Deep manifold learning reveals hidden dynamics of proteasome autoregulation

Zhaolong Wu[1], Shuwen Zhang[1,2], Wei Li Wang[1,3,4], Yinping Ma[1], Yuanchen Dong[5] & Youdong Mao[1-4]*

[1]State Key Laboratory for Mesoscopic Physics, School of Physics, Peking University, Beijing, China. [2]Center for Quantitative Biology, Peking University, Beijing, China. [3]Intel Parallel Computing Center for Structural Biology, Dana-Farber Cancer Institute, Boston, MA, USA. [4]Department of Cancer Immunology and Virology, Dana-Farber Cancer Institute, Department of Microbiology, Harvard Medical School, Boston, MA, USA. [5]Institute of Chemistry, Chinese Academy of Sciences, Beijing, China.

*To whom correspondence may be addressed.

Abstract

The 2.5-MDa 26S proteasome maintains proteostasis and regulates myriad cellular processes[1]. How polyubiquitylated substrate interactions regulate proteasome activity is not understood[1,2]. Here we introduce a deep manifold learning framework, named AlphaCryo4D, which enables atomic-level cryogenic electron microscopy (cryo-EM) reconstructions of nonequilibrium conformational continuum and reconstitutes 'hidden' dynamics of proteasome autoregulation in the act of substrate degradation. AlphaCryo4D integrates 3D deep residual learning[3] with manifold embedding[4] of free-energy landscapes[5], which directs 3D clustering via an energy-based particle-voting algorithm. In blind assessments using simulated heterogeneous cryo-EM datasets, AlphaCryo4D achieved 3D classification accuracy three times that of conventional methods[6-9] and reconstructed continuous conformational changes of a 130-kDa protein at sub-3-Å resolution. By using AlphaCryo4D to analyze a single experimental cryo-EM dataset[2], we identified 64 conformers of the substrate-bound human 26S proteasome, revealing conformational entanglement of two regulatory particles in the doubly capped holoenzymes and their energetic differences with singly capped ones. Novel ubiquitin-binding sites are discovered on the RPN2, RPN10 and α5 subunits to remodel polyubiquitin chains for deubiquitylation and recycle. Importantly, AlphaCryo4D choreographs single-nucleotide-exchange dynamics of proteasomal AAA-ATPase motor during translocation initiation, which upregulates proteolytic activity by allosterically promoting nucleophilic attack. Our systemic analysis illuminates a grand hierarchical allostery for proteasome autoregulation.

The 26S proteasome is the known largest ATP-dependent protease machinery of ~2.5 MDa molecular weight ubiquitously found in all eukaryotic cells. It exists at the center of the ubiquitin-proteasome system (UPS) that regulates myriad cellular processes, such as protein quality control, cell cycle, gene expression, inflammation and immunity[1,2]. Dysregulation of the UPS has been broadly associated with carcinogenesis, ageing, neurodegenerative and cardiovascular diseases[1]. The 26S holoenzyme is assembled by a cylindrical 20S core particle (CP) capped with one or two 19S regulatory particles (RPs), each consisting of the lid and base subcomplexes[1,2]. The ring-like heterohexameric motor of ATPases-associated-with-diverse-cellular-activities (AAA) ATPase in the base subcomplex mechanically unfold polyubiquitylated substrates recognized by ubiquitin receptors in the lid subcomplex. Previous structural data by cryogenic electron microscopy (cryo-EM) have suggested three modes of coordinated ATP hydrolysis in the AAA-ATPase motor that regulate distinct steps of ubiquitin recognition, deubiquitylation, initiation of translocation and processive substrate translocation in the proteasome[2]. However, key intermediate conformations between these states were missing, greatly limiting our understanding of the intrinsic proteasome regulation. The mechanism of the proteasome targeting of substrate-conjugated ubiquitin signals is not fully understood[1,10-12]. How polyubiquitylated substrate interactions regulate proteasome activity remains enigmatic[1].

The 26S proteasome is one of the most complex, dynamic and conformationally heterogeneous holoenzyme machinery in cells[2,13-16], challenging the current approaches in cryo-EM structure determination[6-9,17-19]. Visualizing atomic structures of transient, nonequilibrium intermediates connecting the major states of the proteasome has been unsuccessful by conventional cryo-EM analysis[1,2,9,16,18,19]. To address this major challenge, we developed a novel deep manifold learning system codenamed AlphaCryo4D that can break such a limitation and enable atomic-level cryo-EM reconstructions of highly dynamic, lowly populated intermediates or transient states. By applying AlphaCryo4D to analyze a large cryo-EM dataset that previously solved the atomic structures of 7 proteasomal RP-CP states[2], we reconstructed 64 conformers of the human 26S proteasome in the act of substrate degradation up to 2.5-Å resolution. Systematic analyses of those transient or intermediate states in substrate processing pinpoint energetic differences between the doubly and singly capped proteasomes, discover several novel ubiquitin-binding sites in the proteasome, and choreograph single-nucleotide-exchange dynamics of the proteasomal AAA-ATPase motor during translocation initiation. Importantly, the dramatically

enriched proteasomal states provide unprecedented insights into an integrative, hierarchical allosteric mechanism of proteasome autoregulation upon polyubiquitylated substrate interactions.

Design of deep manifold learning

The conceptual framework of AlphaCryo4D integrates unsupervised 3D deep learning with manifold embedding to learn a free-energy landscape, which directs single-particle cryo-EM reconstructions of rare transient states via an energy-based particle-voting algorithm. In brevity, AlphaCryo4D involves four major steps of data processing (Fig. 1a, Extended Data Fig. 1; see Methods for details): (1) Hundreds to thousands of 3D volumes are bootstrapped with *M*-fold data augmentation by particle shuffling and Bayesian clustering[19], during which each particle is used *M* times in reconstructing *M* volumes; each of the *M* copies is called a 'vote' of the particle (Extended Data Fig. 1a). (2) 3D feature maps of all volumes are learnt by an autoencoder[20] made of a 3D deep residual neural network[3] and are used to compute a free-energy landscape through manifold embedding[4,5] (Fig. 1b, d, e, Extended Data Table 1). (3) A string method[21] is used to search the minimum energy path (MEP) on the free-energy landscape[22], which defines the local energy minima or transition states of interest as the centers of the clustering boundaries for particle voting (Fig. 1f). (4) Each particle is counted for the number of votes that are casted within the voting boundaries on the energy landscape. The particle is classified to the cluster that receives more than *M*/2 votes of this particle within its voting boundary (Fig. 1f, Extended Data Fig. 1b). Particles that cannot be reproducibly voted into any clustering boundaries for more than *M*/2 times are 'voted out' during this procedure. The resulting 3D classes are expected to be conformationally homogeneous enough for high-resolution cryo-EM refinement[8]. Since many protein complexes exhibit profound conformational changes in different local regions, we also implemented a focused classification strategy of AlphaCryo4D that applies a local 3D mask[18] throughout the entire procedure, often being executed as an iterative step after initial 3D classification by AlphaCryo4D in the absence of any 3D mask (Fig. 1a, Methods).

Solving conformational continuum at atomic level

To assess the numerical performance of AlphaCryo4D, we generated three large synthetic heterogeneous cryo-EM datasets with signal-to-noise ratios (SNRs) of 0.05, 0.01 and 0.005. Each dataset includes 2 million randomly oriented single particles computationally simulated

from 20 hypothetical conformer models of the ~130-kDa NLRP3 inflammasome protein[23]. These conformers imitate continuous conformational changes of the NACHT domain rotating around the LRR domain over an angular range of 90° during inflammasome activation[23] (Fig. 1c). We conducted blind assessments on 3D classification and heterogeneous reconstructions by AlphaCryo4D, without providing any information of particle orientation and conformational identities (Fig. 1d-f, Extended Data Fig. 2). The 3D classification precision of a retrieved conformer was computed as the ratio of the particle number of correct class assignment (based on the ground truth) versus the total particle number in the class. The results of AlphaCryo4D were then compared with several conventional methods, including maximum-likelihood-based 3D (ML3D) classification in RELION[8,9,18] and 3D principal component analysis (PCA) in cryoSPARC[7]. In all blind tests, AlphaCryo4D retrieved all 20 conformers and markedly outperformed the conventional methods, with an average of 3D classification precision at 0.83, 0.82 and 0.65 for datasets with SNRs of 0.05, 0.01 and 0.005, respectively (Fig. 2a, Extended Data Fig. 3a-c). By contrast, the conventional methods missed two to six conformers entirely and exhibited 3D classification precisions in the range of 0.2-0.5 in general (Fig. 2b, c, Extended Data Figs. 3d-l, 4).

The 3D classification precision appears to be strongly correlated with the map quality and resolution homogeneity across the density map (Fig. 2). All 20 density maps from AlphaCryo4D consistently show homogeneous resolutions at 2.6-2.9 Å between the NACHT and LRR domains (Fig. 2d, g, Extended Data Figs. 3m, 4a). By contrast, all density maps by the conventional methods show lower average resolutions and notably heterogeneous local resolutions, with the NACHT domain exhibiting substantially lower resolution than that of the LRR domain, causing blurred features, broken loops and invisible sidechains in NACHT (Fig. 2e, f, h, i, Extended Data Figs. 3n, o, 4b, c). Thus, the significantly improved 3D classification accuracy by AlphaCryo4D enables 4D reconstructions of conformational continuum at the atomic level.

To understand how the 3D classification accuracy is improved in AlphaCryo4D, we further studied the algorithmic mechanism by tracking the statistical distributions of classification precisions over intermediate steps of data processing (Extended Data Fig. 5). We found that the steps of particle shuffling, defining cluster boundaries on the manifold-embedded free-energy landscapes and energy-based particle-voting contribute to ~16%, ~20% and ~40% improvements in the distributions of high-precision 3D classes, respectively, suggesting that our design of the

130 particle-voting algorithm considerably improves the performance of AlphaCryo4D, without
131 which deep learning alone is insufficient to achieve the present level of 3D classification
132 accuracy.
133
134 **Visualizing hidden dynamics of the proteasome**
135 Having conducted the proof-of-principle study of AlphaCryo4D using simulated datasets, we
136 then turned to several experimental datasets[2,15]. We first applied this approach to analyze an
137 existing cryo-EM dataset of the substrate-free ATPγS-bound 26S proteasome[15]. The
138 AlphaCryo4D-reconstructed energy landscape clearly shows six local energy minima
139 corresponding to the known six conformational states S_A, S_B, S_C, S_{D1}, S_{D2} and S_{D3}, verifying the
140 applicability of AlphaCryo4D in processing real experimental data[15] (Fig. 3a). Next, we used
141 AlphaCryo4D and its focused classification procedure to analyze a larger cryo-EM dataset of the
142 substrate-engaged 26S proteasome (Fig. 3b, c, Extended Data Fig. 6 and Methods)[2]. This dataset
143 was collected on the human 26S proteasome mixed with a Lys63-linked polyubiquitinated
144 substrate $Sic1^{PY}$ for 30 seconds before ATP was diluted with ATPγS, which was expected to
145 maximally capture any intermediate states before the degradation reaction was completed[2]. The
146 reconstruction of the free energy landscape of the substrate-engaged proteasome suggests that the
147 rate-limiting step of substrate degradation lies in the initiation of substrate unfolding after
148 substrate deubiquitylation, reflected in the highest activation energy barrier between states E_B
149 and E_{C1} (Fig. 3b, c), consistent with a recent fluorescence microscopy study on the proteasome
150 kinetics[24].
151 Impressively, AlphaCryo4D extracted significantly more conformers of the proteasomes in
152 various forms from the same cryo-EM dataset that previously yielded seven atomic structures of
153 the proteasome[2]. It discovered 20 conformational states of RP-CP subcomplex (Fig. 3b, c,
154 Extended Data Fig. 7, Extended Data Table 2). Eight transient states (designated $E_{A1.2}$, $E_{A2.2}$,
155 $E_{A2.3}$, $E_{B.2}$, $E_{B.3}$, $E_{D2.2}$, $E_{D2.3}$ and $E_{D.\alpha5}$) at 3.1-7.5 Å resolution exhibit previously unseen features
156 of ubiquitin that map various ubiquitin-binding sites on the RPN1, RPN2, RPN10 and α5
157 subunits in the proteasome (Fig. 4). Six sequential intermediate states (designated $E_{D0.1}$, $E_{D0.2}$,
158 $E_{D0.3}$, $E_{D1.1}$, $E_{D1.2}$ and $E_{D1.3}$) at 3.2-3.9 Å resolution bridge a major missing gap between states
159 E_{C2} and E_{D1}, revealing how concerted structural transitions in the AAA-ATPase motor during

single-nucleotide exchange drive the initiation of substrate unfolding (Fig. 5, Extended Data Fig. 7c, g-i).

To understand whether the singly capped (SC) and doubly capped (DC) proteasomes behave differently, AlphaCryo4D reconstructed 8 and 36 conformational states for the pure SC and DC holoenzymes, respectively (Fig. 3d, e, Extended Data Figs. 8, 9). All 8 SC and 29 DC states were refined to 3.7-4.7 Å, with 7 DC states limited to 6-9 Å due to their transient nature and extremely low population (Extended Data Fig. 8b, e, f). Note that the CP gate in the RP-distal side of the 20 states of RP-CP subcomplex is in a heterogeneous conformation of various stoichiometric ratios between closed and open states. By contrast, both CP gates in the 44 states of pure SC or DC reconstructions are in a homogeneous conformation.

Besides resolving significantly more conformers, AlphaCryo4D pushes the envelope of the achievable resolution of known states due to its advantage in keeping more particles without sacrificing conformational homogeneity. For example, the structure of state E_{D2} was improved from previous resolution at 3.2 Å to 2.5 Å, allowing us to investigate how the CP gating allosterically regulates the catalytic activity of the β-type subunits (Fig. 6, Extended Data Fig. 7c, g-i). The local resolution of RPN11-bound ubiquitin in state E_{A2} was also improved from 5-6 Å to 3.5 Å among many other improvements (Extended Data Fig. 10a).

Conformational entanglement

Both the SC and DC proteasomes are abundant in cells[25]. Their structural and functional difference, however, remains elusive. In the 36 DC reconstructions, each conformer is a combination of two RP states. Each CP gate in the DC proteasome appears to be rigorously controlled by their respective proximal RP and is only open when its proximal RP is in an E_D-compatible state with five RPT C-terminal tails inserted into the surface pockets on the α-ring[2] (Fig. 3e, Extended Data Fig. 8a-d). Consistently, the gate on the RP-free side of the CP in the SC proteasome is closed in all states, indicating the CP gate opening on the RP-controlled side does not remotely open the other CP gate on the RP-free side (Extended Data Fig. 8d).

To understand whether the conformational states of two RPs in the DC proteasome allosterically influence each other, we compare the state distribution matrix obtained by AlphaCryo4D to the prediction of a control model assuming two completely uncoupled RP states in the DC proteasome (Fig. 3f-h). Although the overall pattern of the experimental distribution

191 roughly agrees with the model prediction, a notable number of DC states exhibit substantial
192 deviation, indicating that the conformational dynamics of the two RPs in the same proteasome
193 are profoundly entangled together (Fig. 3g, h). Intriguingly, the most prominent positive
194 deviations are seen in the state distributions of E_B-E_B, E_B-E_{D2}, and E_{D2}-E_{D2} combinations (Fig.
195 3g), suggesting that the deubiquitylation state E_B and the translocation state E_{D2} of one RP are
196 allosterically coupled to and mutually upregulated by states E_B and E_{D2} of the opposite RP.
197 Coupled actions of deubiquitylation and translocation between two opposite RPs are expected to
198 optimize the efficiency of substrate processing. Moreover, all the DC states along the diagonal of
199 the state distribution matrix are more or less upregulated (indicated by red in Fig. 3g, h),
200 suggesting that both RPs in the same proteasome synergistically promote each other to transit
201 into downstream states in a symmetrical fashion.
202 Notably, the largest discrepancy of the distribution of RP states between the SC and DC
203 proteasomes also lies in state E_B (Fig. 3b-d). The state population of E_B is significantly lower in
204 the SC than in the DC proteasome. This observation verifies the conclusion drawn from the
205 above analysis on the DC proteasomes alone that state E_B is upregulated by the conformational
206 entanglement effect in the DC holoenzyme, suggesting that the SC proteasome lacks the
207 functional synergy between two opposite RPs seen in the DC proteasome (Fig. 3h). Altogether,
208 these results implicate that the DC proteasome could be energetically more efficient in substrate
209 deubiquitylation and degradation than the SC proteasome.
210
211 **Novel ubiquitin-binding sites**
212 Unexpectedly, in states $E_{A1.2}$, $E_{A2.2}$, and $E_{B.2}$, a diubiquitin-like density is consistently found on
213 RPN2, whereas a monoubiquitin-like density is observed at the apex of the von Willebrand
214 factor type A (VWA) domain of RPN10 in states $E_{A2.3}$, $E_{B.3}$ and $E_{D2.3}$ (Fig. 4a, Extended Data
215 Fig. 10b-f). In state $E_{D2.2}$, the diubiquitin-like density, however, appears to contact both RPN2
216 and RPN10, and can be modelled with a Lys63-linked diubiquitin (Extended Data Fig. 10b, f).
217 The RPN10 ubiquitin-interacting motifs (UIMs), however, were not reliably observed
218 presumably due to their highly flexible nature (Extended Data Fig. 10f). The populations of these
219 states are very small and represented in only a few thousand particles or 0.1-0.3% of the entire
220 dataset, indicating their transient nature. The local resolutions of the RPN2- and RPN10-bound
221 ubiquitin-like densities are lower than the rest of the reconstructions and other ubiquitin densities

222 on RPN1, RPN11 and α5 subunits. Rigid-body fitting of the ubiquitin structure into these
223 ubiquitin-like densities confirms the agreement of the overall density shape with the ubiquitin
224 structure (Fig. 4a, Extended Data Fig. 10b, c, f).

225 The ubiquitin-binding site on RPN2 is centered on three helices harboring an acidic surface
226 around residues Tyr502, Glu530, Asp531 and Ser569 (Fig. 4b-e). Structural comparison suggests
227 that the ubiquitin-binding site on RPN2 is homologous to the T1 site of RPN1 (Fig. 4c, d)[12]. We
228 therefore name it 'the RPN2 T1 site'. Although there is little conservation in amino acid
229 sequences between the RPN1 and RPN2 T1 sites, their structural and electrostatic properties are
230 highly conserved (Fig. 4d, Extended Data Fig. 10g-j). Comparison with the NMR structure of
231 Lys48-linked diubiquitin-bound RPN1 T1 site helices[12] further confirms the conservation and
232 similarity of the ubiquitin-binding modes between the RPN1 and RPN2 T1 sites (Fig. 4c).
233 Consistent with this finding, previous studies have observed weak interactions of ubiquitin-like
234 (UBL) protein with RPN2 by cross-linking experiments[26]. As there is also ubiquitin bound to
235 RPN11 in states $E_{A2.2}$, and $E_{B.2}$, a Lys63-linked triubiquitin chain can be fitted into the RPN2-
236 and RPN11-bound ubiquitin densities by modeling the rotation of Lys63 linkages, suggesting
237 that the RPN2 T1 site may function as a coreceptor site for ubiquitin transfer from RPN10 to
238 RPN11 to facilitate deubiquitylation (Fig. 4g). Given that at least one RPN10 UIM-bound
239 ubiquitin invisible in these cryo-EM maps would be expected to exist, the observation of
240 triubiquitin on RPN2 and RPN11 structurally rationalizes why tetraubiquitin is an optimal
241 degradation signal for the proteasome[1].

242 By focused 3D classification via AlphaCryo4D, we refined the RPN1 with ubiquitin binding
243 its T2 site[12] in state E_{A1} to 3.7 Å, which was previously reconstructed at moderate resolution (~5
244 Å) (Extended Data Fig. 10d). This allows us to visualize the RPN1 T2 site in atomic detail,
245 revealing that the ubiquitin-contacting surface is composed of residues Asp423, Leu426,
246 Asp430, Glu458, Cys459, and Asp460 from two helices (Fig. 4c, d), representing a footprint that
247 is slightly larger than the yeast Rpn1 T2 site for Ubp6 interaction[12]. Previous data have suggested
248 that RPN1 T2 site is a receptor site for UBL proteins like Ubp6 and USP14 with lack of evidence
249 for ubiquitin binding[12]. Our direct observation of ubiquitin binding at this site revises such a
250 conception, suggesting that the RPN1 T2 may be also a primary ubiquitin receptor site.

251 In state $E_{D2.2}$, we can observe a ubiquitin density bound to the RPN1 T2 site and another
252 weaker ubiquitin density at the α5-subunit ~6 nm beneath the RPN1 T2 site (Fig. 4a, Extended

253 Data Fig. 10b). To understand if the ubiquitin-binding site on the α5 subunit is used more
254 broadly, we combined all the E_D-compatible states and focused the 3D classification of
255 AlphaCryo4D on the α5-bound ubiquitin. This yielded a much larger 3D class, named state $E_{D.\alpha5}$
256 (~4% of the entire dataset) that improved the ubiquitin-bound CP structure to 3.1 Å, and the α5-
257 bound ubiquitin density to 4-4.5 Å (Extended Data Figs. 7e,). The ubiquitin-binding site in the
258 α5 subunit is composed of acidic or hydrophobic residues Glu183, Val184, His186, Ser188 and
259 Glu193 in a loop connecting two helices, highly resembling the mode of ubiquitin binding to an
260 RPN13 loop[11,27] (Fig. 4f, Extended Data Fig. 10e). The electrostatic property of this site is also
261 similar to those of the RPN1 T1, T2 and RPN2 T1 sites that are all acidic, in charge
262 complementarity with the basic ubiquitin surface around residues Ile44 and His68 (Extended
263 Data Fig. 10g-n).
264 We note that these new ubiquitin-binding sites all reside in the vicinity of primary receptor
265 sites. The RPN2 T1 site is very close to the RPN10 UIMs, whereas the α5 site is near the RPN1
266 T2 site. Modelling of a Lys63-linked tetraubiquitin chain by fitting its terminal ubiquitin into the
267 cryo-EM density suggests that a single tetraubiquitin can span across the α5 subunit and the
268 RPN1 T2 site (Fig. 4h). Given that RPN1 appears to allosterically regulate the AAA-ATPase
269 motor conformation[2] (Fig. 5a, b), tetraubiquitin binding to both the RPN1 T2 site and α5 subunit
270 could allosterically stabilize the open-CP states (E_{D0}, E_{D1} and E_{D2}). It is unclear whether these
271 low-affinity ubiquitin-binding sites would directly involve in primary targeting of substrate-
272 conjugated polyubiquitin chains by the proteasome in cells. However, it is conceivable that the
273 polyubiquitin chains could be first captured by the high-affinity sites and then moved to the
274 nearby low-affinity sites. Working together, these ubiquitin-binding sites could remodel
275 polyubiquitin chains and deliver the peptide-proximal ubiquitin to the deubiquitylation site[2] (Fig.
276 4g) as well as assist ubiquitin recycle after isopeptide bond hydrolysis (Fig. 4h). We expect that
277 our structural definition of these novel ubiquitin-binding sites would stimulate future functional
278 tests required to understand their biological importance in cells.
279
280 **Single-nucleotide exchange dynamics**
281 The six intermediate states ($E_{D0.1}$, $E_{D0.2}$, $E_{D0.3}$, $E_{D1.1}$, $E_{D1.2}$ and $E_{D1.3}$) during initiation of substrate
282 unfolding and translocation exhibit highly coordinated movements in the RP relative to the CP
283 (Fig. 5a-c, Extended Data Fig. 11), with prominent rotations in the RPN1 N-terminal that

284 detaches from RPT6 in states $E_{D0.1}$, $E_{D0.2}$, and $E_{D0.3}$ and re-binds RPT6 in state $E_{D1.1}$, $E_{D1.2}$ and
285 $E_{D1.3}$. All six conformations share the same architecture in their substrate interactions with pore-1
286 loops from four RPT subunits (RPT2, RPT6, RPT3 and RPT4), which remain largely unchanged
287 in overall conformation (Fig. 5d). These structures illustrate that the RPT2 re-association with
288 the substrate proceeds that of RPT1 after both RPT1 and RPT2 are dissociated from the substrate
289 in state E_C. They also share the same pattern of nucleotide states, with ATP bound to RPT1,
290 RPT2, RPT6 and RPT3 and ADP bound to RPT4. There are poor, partial nucleotide densities in
291 the RPT5 nucleotide-binding pocket, which give rise to the highest B-factor (250-500) when
292 fitted with ADP, suggesting that RPT5 undergoes ADP release in these states (Extended Data
293 Fig. 11k).
294 Markedly, the pore-1 loop of RPT1 gradually moves toward the substrate from a distance of
295 ~16 Å to ~3 Å, whereas the pore-1 loop of RPT5 gradually moves away from the substrate from
296 a distance of ~3 Å to ~16 Å (Fig. 5d, f). The small AAA subdomain of RPT5 moves inward
297 together with the large AAA subdomain of RPT1, as the large AAA subdomain of RPT5 rotates
298 away from the substate (Extended Data Fig. 11f-i). Consistently, the arginine fingers (R-finger)
299 of RPT2 are progressively moved toward ATP bound in RPT1, closing up the nucleotide-binding
300 pocket (Fig. 5e, g). In contrast, the nucleotide-binding pocket of RPT5 is gradually shrunk but is
301 not fully closed by the R-fingers of RPT1, whereas the nucleotide-binding pocket of RPT4 is
302 gradually opened up (Fig. 5g). As a result, the pore-1 loops of RPT1 and RPT5 are only in
303 contact with the substate in the last and first states $E_{D1.3}$ and $E_{D0.1}$, respectively. Both are
304 dissociated from the substate in states $E_{D0.2}$, $E_{D0.3}$, $E_{D1.1}$, and $E_{D1.2}$. These gradual movements
305 allow us to assign their temporal sequences as illustrated (Fig. 5a-e), indicating that these states
306 represent intermediate conformations accompanying single-nucleotide exchange that occurs in
307 the RPT5 (Fig. 5h). Interestingly, the outward flipping of RPT5 appears to complete its major
308 conformational change in state $E_{D0.3}$, much faster than the inward motion of RPT1, which
309 completes its conformational change in state $E_{D1.3}$. This observation suggests that ATPase re-
310 engagement with the substrate is the rate-limiting step in the single-nucleotide exchange kinetics
311 of the AAA-ATPase motor.
312 Our data clarify that the CP gate is open once the pore-1 loop of RPT2 binds the substrate in
313 state $E_{D0.1}$, as five RPT C-tails are inserted in the α-pockets in all six states (Extended Data Fig.
314 8c). Altogether, these structures vividly characterize at the atomic level how the "hand-over-

315 hand" actions of RPT subunits are executed by coordinated conformational dynamics in the
316 AAA-ATPase motor during single-nucleotide exchange and generates mechanical force
317 unfolding the substrate. Although the sequential model of coordinated ATP hydrolysis around
318 the AAA-ATPase ring has been hypothesized in numerous similar systems[1,2,13,16,28], our results
319 provide the first direct evidence for sequential intermediate states of hand-over-hand actions
320 within a single cycle of nucleotide exchange.
321

322 **Hierarchical allosteric regulation of proteolytic activity**

323 Both atomic structures of the substrate-bound CPs in the open- and closed-gate states E_A and E_{D2}
324 show a segment of substrate polypeptide binding the catalytically active residue Thr1 in the β2
325 subunit, whereas no substrate density is observed in the other two catalytic subunits β1 and β5.
326 In both states, the substrate is bound in a β-sheet conformation between residues 20 to 22 and 46
327 to 48 in the β2 subunit (Fig. 6a, b, Extended Data Fig. 12), reminiscent of the conformations of
328 CP inhibitors binding the β5 subunits in the crystal structures of the CP[29,30]. The hydroxyl
329 oxygen atom in the catalytic Thr1 is ~2-Å closer to the substrate mainchain in state E_{D2}
330 compared to state E_A. This structural difference is expected to result from the CP gate opening
331 that exerts a profound allosteric impact on the entire CP structure.

332 To understand how such a subtle structural change influences the proteolytic activity, we
333 carried out first-principles calculations of the quantum-mechanical interactions involved in the
334 nucleophilic attack of the catalytic residue Thr1 on the scissile peptide bond in the substrate,
335 using the density functional theory (DFT) with the generalized gradient approximation[31]. To
336 initiate the nucleophilic attack, the carbonyl group needs to be bought to the proximity of the
337 electrophile Thr1-Oγ to facilitate the quantum-mechanical interactions[32,33]. We calculated the
338 charge density difference induced around the interacting pair after proton transfer from Thr1-Oγ
339 to Thr1-NH_2 and plotted the contour maps (Fig. 6c, d, Extended Data Fig. 12e, f). It is seen that
340 the substrate-interacting pair of atoms in state E_{D2} start to form a bonding region of slight
341 positive charge difference linking the carbonyl group of the substrate and the Thr1-Oγ. By
342 contrast, the pair are too far apart to interact and are well separated by a charge depletion non-
343 bonding region in state E_A. Indeed, a recent study has found that the nucleophilic attack is the
344 rate-limiting step in the acylation barrier using the yeast CP structure in the gate-closed state[33].
345 Our result suggests that CP gate opening allosterically promotes the nucleophilic attack by

346 lowering the activation energy barrier of acylation and induces hybridization of the molecular
347 orbitals, hence upregulating the reaction rate of proteolysis. In support of our structural finding,
348 previous studies have observed indirect evidence for coupling of the CP gating with the
349 proteolytic activity[34,35].

350 Taken together, our systematic structural analyses point to a grand allostery model for the
351 proteasomal autoregulation of proteolytic activity through a three-tier hierarchy of inter-
352 molecular interaction networks (Fig. 6e), in which all subunit conformations are allosterically
353 coupled. The first tier of autoregulation is between the CP gate in the α-ring and the catalytic
354 sites of the β-subunits. Opening of the CP gate allosterically upregulates the proteolytic activity
355 of the three β-subunits. The second tier of autoregulation lies between the substrate-bound AAA-
356 ATPase motor and the rest of the proteasome. The AAA-ATPase motor bridges the ubiquitin-
357 binding sites and the CP via direct interactions of the RPT coiled-coil (CC) domains with RPN1,
358 RPN2 and RPN10 harboring ubiquitin-binding sites. As a result, three modes of coordinated
359 ATP hydrolysis appear to regulate the intermediate steps of substrate processing[1,2], in which
360 initiation of substrate unfolding is allosterically coupled with CP gating during E_{C2} to $E_{D0.1}$
361 transition (Fig. 5). The third tier of autoregulation is via dynamic interactions between ubiquitin
362 signals and a collection of ubiquitin receptor sites and deubiquitinases. This is manifested as the
363 dual roles of ubiquitin-binding sites in recognizing ubiquitin signals and in transmitting such
364 recognitions to allosteric regulation of AAA-ATPase conformations that control the CP gate.
365 Ubiquitin binding and remodeling destabilizes the resting state of the proteasome and promotes
366 its transition to states E_B, E_C and ultimately E_D. On the other hand, a polyubiquitin chain binding
367 multiple sites in the proteasome could have profound allosteric and conformational selection
368 effects (Fig. 4g, h). Such three-tier, hierarchical allosteric regulations may occur mutually with
369 both RPs and are expected to underlie the conformational entanglement of the two RPs in the DC
370 proteasome (Fig. 3e), which was not clearly observed in the absence of substrates[15,36]. This grand
371 allostery mechanism might have been evolved to optimize the proteasome function in response
372 to extremely complicated intracellular challenges and is manifested as various phenotypic
373 effects, such as UBL-induced proteasome activation[37,38], long-range allosteric regulation of RP
374 by CP inhibitors[35] and allosteric coupling of two opposite α-ring gates in the archaeal CP[39].
375

376 **Concluding remarks**

In this work, motivated by solving the hidden dynamics of proteasome autoregulation, we developed AlphaCryo4D, a novel framework of deep manifold learning, that enables 3D reconstructions of nonequilibrium conformational continuum at the atomic level. In retrospective, finding novel ubiquitin-binding sites in the proteasome, choreographing sequential intermediates within a single cycle of nucleotide exchange, and detecting conformational entanglement of the two RPs in the DC holoenzyme as well as subtle allosteric effects of polypeptide hydrolysis by CP gating, each itself presents a formidable challenge. Being able to accomplish all these missions on a single experimental dataset by solving 64 proteasomal states demonstrates that AlphaCryo4D is a major advancement of deep learning in solving 3D heterogeneity problems in cryo-EM structure analysis and showcases tremendous potentials of deep learning in transforming cryo-EM and molecular imaging. More importantly, AlphaCryo4D revealed 'previously invisible' mechanistic details in nonequilibrium transient interactions of the proteasome with polyubiquitylated substrates and offered unprecedented insights into the grand hierarchical allostery underlying the proteasome activity and function. With recent improvements in cryo-EM instruments[40,41] and time-resolved sample preparation methods[42,43], we expect that current development and future widespread applications of AlphaCryo4D or similar approaches will considerably boost the capability of cryo-EM imaging as a de novo discovery tool and transform modern research in physical and molecular biology.

References

1 Mao, Y. Structure, Dynamics and Function of the 26S Proteasome. In: Harris J.R., Marles-Wright J. (eds) Macromolecular Protein Complexes III: Structure and Function. *Subcell Biochem* **96**, 1-151, doi:10.1007/978-3-030-58971-4_1 (2021).

2 Dong, Y. *et al.* Cryo-EM structures and dynamics of substrate-engaged human 26S proteasome. *Nature* **565**, 49-55, doi:10.1038/s41586-018-0736-4 (2019).

3 He, K., Zhang, X., Ren, S. & Sun, J. Deep Residual Learning for Image Recognition. *2016 IEEE Conference on Computer Vision and Pattern Recognition (CVPR), Las Vegas, NV*, 770-778, doi:10.1109/CVPR.2016.90 (2016).

4 van der Maaten, L. & Hinton, G. Visualizing Data using t-SNE. *J Mach Learn Res* **9**, 2579-2605 (2008).

5 Dashti, A. *et al.* Trajectories of the ribosome as a Brownian nanomachine. *Proc Natl Acad Sci U S A* **111**, 17492-17497, doi:10.1073/pnas.1419276111 (2014).

6 Frank, J. *Three-dimensional electron microscopy of macromolecular assemblies : visualization of biological molecules in their native state*. 2nd edn, (Oxford University Press, 2006).

7 Punjani, A., Rubinstein, J. L., Fleet, D. J. & Brubaker, M. A. cryoSPARC: algorithms for rapid unsupervised cryo-EM structure determination. *Nat Methods* **14**, 290-296,

414 doi:10.1038/nmeth.4169 (2017).
415 8 Zivanov, J. *et al.* New tools for automated high-resolution cryo-EM structure
416 determination in RELION-3. *Elife* **7**, doi:10.7554/eLife.42166 (2018).
417 9 Nakane, T., Kimanius, D., Lindahl, E. & Scheres, S. H. Characterisation of molecular
418 motions in cryo-EM single-particle data by multi-body refinement in RELION. *Elife* **7**,
419 doi:10.7554/eLife.36861 (2018).
420 10 Galves, M., Rathi, R., Prag, G. & Ashkenazi, A. Ubiquitin Signaling and Degradation of
421 Aggregate-Prone Proteins. *Trends Biochem Sci*, doi:10.1016/j.tibs.2019.04.007 (2019).
422 11 Husnjak, K. *et al.* Proteasome subunit Rpn13 is a novel ubiquitin receptor. *Nature* **453**,
423 481-488, doi:10.1038/nature06926 (2008).
424 12 Shi, Y. *et al.* Rpn1 provides adjacent receptor sites for substrate binding and
425 deubiquitination by the proteasome. *Science* **351**, doi:10.1126/science.aad9421 (2016).
426 13 Zhang, S. & Mao, Y. AAA+ ATPases in Protein Degradation: Structures, Functions and
427 Mechanisms. *Biomolecules* **10**, doi:10.3390/biom10040629 (2020).
428 14 Chen, S. *et al.* Structural basis for dynamic regulation of the human 26S proteasome.
429 *Proc Natl Acad Sci U S A* **113**, 12991-12996, doi:10.1073/pnas.1614614113 (2016).
430 15 Zhu, Y. *et al.* Structural mechanism for nucleotide-driven remodeling of the AAA-
431 ATPase unfoldase in the activated human 26S proteasome. *Nat Commun* **9**, 1360,
432 doi:10.1038/s41467-018-03785-w (2018).
433 16 de la Pena, A. H., Goodall, E. A., Gates, S. N., Lander, G. C. & Martin, A. Substrate-
434 engaged 26S proteasome structures reveal mechanisms for ATP-hydrolysis-driven
435 translocation. *Science* **362**, doi:10.1126/science.aav0725 (2018).
436 17 Wu, J. *et al.* Massively parallel unsupervised single-particle cryo-EM data clustering via
437 statistical manifold learning. *PLoS One* **12**, e0182130, doi:10.1371/journal.pone.0182130
438 (2017).
439 18 Scheres, S. H. Processing of Structurally Heterogeneous Cryo-EM Data in RELION.
440 *Methods Enzymol* **579**, 125-157, doi:10.1016/bs.mie.2016.04.012 (2016).
441 19 Scheres, S. H. *et al.* Disentangling conformational states of macromolecules in 3D-EM
442 through likelihood optimization. *Nat Methods* **4**, 27-29, doi:10.1038/nmeth992 (2007).
443 20 Hinton, G. E. & Salakhutdinov, R. R. Reducing the dimensionality of data with neural
444 networks. *Science* **313**, 504-507, doi:10.1126/science.1127647 (2006).
445 21 E, W., Ren, W. & Vanden-Eijnden, E. String method for the study of rare events. *Phys*
446 *Rev B* **66**, 052301 (2002).
447 22 E, W., Ren, W. & Vanden-Eijnden, E. Simplified and improved string method for
448 computing the minimum energy paths in barrier-crossing events. *J Chem Phys* **126**,
449 164103, doi:10.1063/1.2720838 (2007).
450 23 Sharif, H. *et al.* Structural mechanism for NEK7-licensed activation of NLRP3
451 inflammasome. *Nature* **570**, 338-343, doi:10.1038/s41586-019-1295-z (2019).
452 24 Bard, J. A. M., Bashore, C., Dong, K. C. & Martin, A. The 26S Proteasome Utilizes a
453 Kinetic Gateway to Prioritize Substrate Degradation. *Cell* **177**, 286-298 e215,
454 doi:10.1016/j.cell.2019.02.031 (2019).
455 25 Asano, S. *et al.* Proteasomes. A molecular census of 26S proteasomes in intact neurons.
456 *Science* **347**, 439-442, doi:10.1126/science.1261197 (2015).
457 26 Saeki, Y., Sone, T., Toh-e, A. & Yokosawa, H. Identification of ubiquitin-like protein-
458 binding subunits of the 26S proteasome. *Biochem Biophys Res Commun* **296**, 813-819,
459 doi:10.1016/s0006-291x(02)02002-8 (2002).

27 Schreiner, P. *et al.* Ubiquitin docking at the proteasome through a novel pleckstrin-homology domain interaction. *Nature* **453**, 548-552, doi:10.1038/nature06924 (2008).
28 Puchades, C., Sandate, C. R. & Lander, G. C. The molecular principles governing the activity and functional diversity of AAA+ proteins. *Nat Rev Mol Cell Biol* **21**, 43-58, doi:10.1038/s41580-019-0183-6 (2020).
29 Lowe, J. *et al.* Crystal structure of the 20S proteasome from the archaeon T. acidophilum at 3.4 A resolution. *Science* **268**, 533-539, doi:10.1126/science.7725097 (1995).
30 Schrader, J. *et al.* The inhibition mechanism of human 20S proteasomes enables next-generation inhibitor design. *Science* **353**, 594-598, doi:10.1126/science.aaf8993 (2016).
31 Perdew, J. P., Burke, K. & Ernzerhof, M. Generalized Gradient Approximation Made Simple. *Phys Rev Lett* **77**, 3865-3868, doi:10.1103/PhysRevLett.77.3865 (1996).
32 Groll, M. *et al.* Structure of 20S proteasome from yeast at 2.4 A resolution. *Nature* **386**, 463-471, doi:10.1038/386463a0 (1997).
33 Saha, A., Oanca, G., Mondal, D. & Warshel, A. Exploring the Proteolysis Mechanism of the Proteasomes. *J Phys Chem B* **124**, 5626-5635, doi:10.1021/acs.jpcb.0c04435 (2020).
34 Osmulski, P. A., Hochstrasser, M. & Gaczynska, M. A tetrahedral transition state at the active sites of the 20S proteasome is coupled to opening of the alpha-ring channel. *Structure* **17**, 1137-1147, doi:10.1016/j.str.2009.06.011 (2009).
35 Haselbach, D. *et al.* Long-range allosteric regulation of the human 26S proteasome by 20S proteasome-targeting cancer drugs. *Nat Commun* **8**, 15578, doi:10.1038/ncomms15578 (2017).
36 Eisele, M. R. *et al.* Expanded Coverage of the 26S Proteasome Conformational Landscape Reveals Mechanisms of Peptidase Gating. *Cell Rep* **24**, 1301-1315 e1305, doi:10.1016/j.celrep.2018.07.004 (2018).
37 Collins, G. A. & Goldberg, A. L. Proteins containing ubiquitin-like (Ubl) domains not only bind to 26S proteasomes but also induce their activation. *Proc Natl Acad Sci U S A* **117**, 4664-4674, doi:10.1073/pnas.1915534117 (2020).
38 Kim, H. T. & Goldberg, A. L. UBL domain of Usp14 and other proteins stimulates proteasome activities and protein degradation in cells. *Proc Natl Acad Sci U S A* **115**, E11642-E11650, doi:10.1073/pnas.1808731115 (2018).
39 Yu, Z. *et al.* Allosteric coupling between alpha-rings of the 20S proteasome. *Nat Commun* **11**, 4580, doi:10.1038/s41467-020-18415-7 (2020).
40 Nakane, T. *et al.* Single-particle cryo-EM at atomic resolution. *Nature* **587**, 152-156, doi:10.1038/s41586-020-2829-0 (2020).
41 Yip, K. M., Fischer, N., Paknia, E., Chari, A. & Stark, H. Atomic-resolution protein structure determination by cryo-EM. *Nature* **587**, 157-161, doi:10.1038/s41586-020-2833-4 (2020).
42 Dandey, V. P. *et al.* Time-resolved cryo-EM using Spotiton. *Nat Methods* **17**, 897-900, doi:10.1038/s41592-020-0925-6 (2020).
43 Kaledhonkar, S. *et al.* Late steps in bacterial translation initiation visualized using time-resolved cryo-EM. *Nature* **570**, 400-404, doi:10.1038/s41586-019-1249-5 (2019).
44 Zhu, Y., Ouyang, Q. & Mao, Y. A deep convolutional neural network approach to single-particle recognition in cryo-electron microscopy. *BMC Bioinformatics* **18**, 348, doi:10.1186/s12859-017-1757-y (2017).
45 Bepler, T. *et al.* Positive-unlabeled convolutional neural networks for particle picking in cryo-electron micrographs. *Res Comput Mol Biol* **10812**, 245-247 (2018).

46 Qian, N. On the momentum term in gradient descent learning algorithms. *Neural Netw* **12**, 145-151, doi:10.1016/s0893-6080(98)00116-6 (1999).
47 Unverdorben, P. *et al.* Deep classification of a large cryo-EM dataset defines the conformational landscape of the 26S proteasome. *Proc Natl Acad Sci U S A* **111**, 5544-5549, doi:10.1073/pnas.1403409111 (2014).
48 Wehmer, M. *et al.* Structural insights into the functional cycle of the ATPase module of the 26S proteasome. *Proc Natl Acad Sci U S A* **114**, 1305-1310, doi:10.1073/pnas.1621129114 (2017).
49 Emsley, P. & Cowtan, K. Coot: model-building tools for molecular graphics. *Acta Crystallogr D Biol Crystallogr* **60**, 2126-2132, doi:10.1107/S0907444904019158 (2004).
50 Pettersen, E. F. *et al.* UCSF Chimera--a visualization system for exploratory research and analysis. *J Comput Chem* **25**, 1605-1612, doi:10.1002/jcc.20084 (2004).
51 Adams, P. D. *et al.* PHENIX: a comprehensive Python-based system for macromolecular structure solution. *Acta Crystallogr D Biol Crystallogr* **66**, 213-221, doi:10.1107/S0907444909052925 (2010).
52 The PyMOL Molecular Graphics System Version 2.0 (Schrödinger, LLC).
53 Goddard, T. D. *et al.* UCSF ChimeraX: Meeting modern challenges in visualization and analysis. *Protein Sci* **27**, 14-25, doi:10.1002/pro.3235 (2018).
54 Kucukelbir, A., Sigworth, F. J. & Tagare, H. D. Quantifying the local resolution of cryo-EM density maps. *Nat Methods* **11**, 63-65, doi:10.1038/nmeth.2727 (2014).
55 Heymann, J. B. & Belnap, D. M. Bsoft: image processing and molecular modeling for electron microscopy. *J Struct Biol* **157**, 3-18, doi:10.1016/j.jsb.2006.06.006 (2007).
56 Dolinsky, T. J., Nielsen, J. E., McCammon, J. A. & Baker, N. A. PDB2PQR: an automated pipeline for the setup of Poisson-Boltzmann electrostatics calculations. *Nucleic Acids Res* **32**, W665-667, doi:10.1093/nar/gkh381 (2004).
57 Soler, J. M. *et al.* The SIESTA method for ab initio order-N materials simulation. *J Phys Condens Matter* **14**, 2745-2779 (2002).

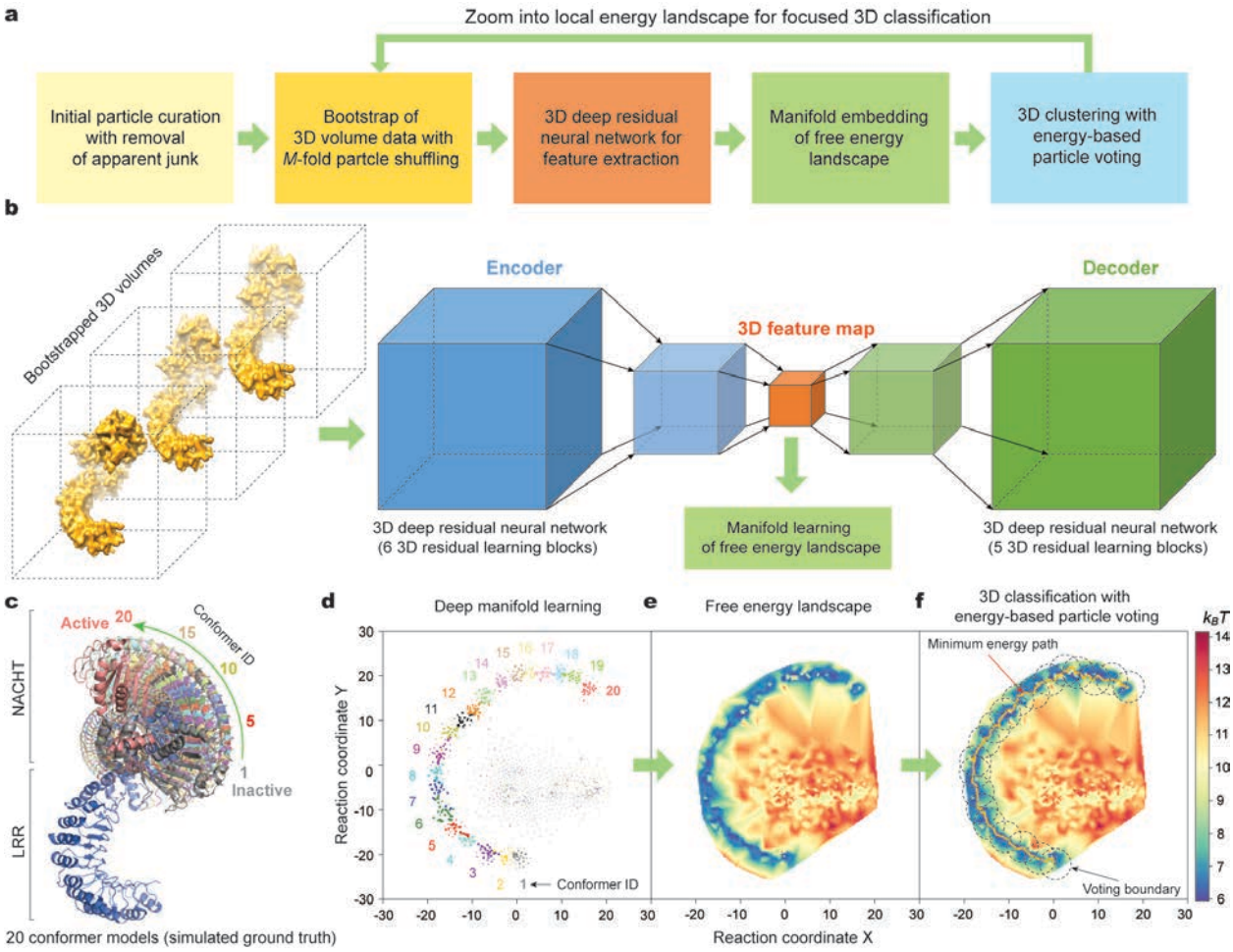

Figure 1. Conceptual framework of AlphaCryo4D for 4D cryo-EM reconstruction. a, Schematic showing the major conceptual steps of single-particle cryo-EM data processing in AlphaCryo4D. **b**, Illustration of deep residual learning of 3D feature maps by an autoencoder conjugated to a decoder for unsupervised training. **c**, The 20 atomic models of hypothetical conformers of NLRP3 in cartoon representations simulate a 90° rotation of the NACHT domain relative to the LRR domain based on the structure of NLRP3 (PDB ID: 6NPY). **d**, Manifold learning of the bootstrapped 3D volumes and their feature maps learnt by the autoencoder. Each data point corresponds to a 3D volume. The color labels the conformer identity of ground truth for the purpose of verification. **e**, Free energy landscape computed from the manifold shown in **d** using the Boltzmann distribution. **f**, Minimum energy path (orange line) calculated by the string method is used to find the approximate cluster centers of 20 conformers. The cluster boundaries for energy-based particle voting are shown as dashed circles.

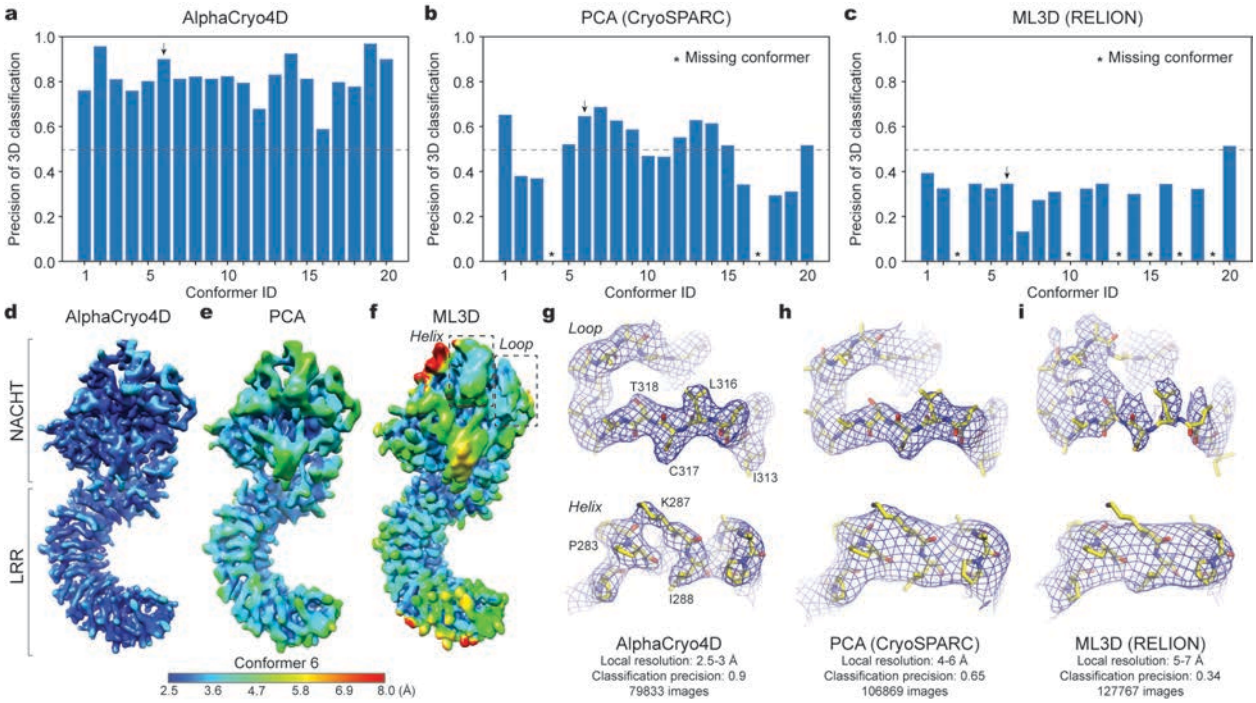

Figure 2. Performance evaluation of AlphaCryo4D for sub-3-Å reconstructions of conformational continuum. **a-c**, Plots of 3D classification precisions of the 20 NLRP3 conformers from blind assessments on the simulated NLRP3 dataset with SNR of 0.01, using AlphaCyo4D (**a**), PCA-based clustering implemented in CryoSPARC (**b**) and 3D maximum-likelihood (ML3D) method implemented in RELION (**c**). All 3D conformers in panel (a) were reconstructed to 2.6-2.9 Å resolution (Extended Data Fig. 3m). Asterisks mark the missing conformers that were completely lost due to misclassification by PCA and ML3D. **d-f**, Typical side-by-side comparison of density map quality and local resolution of the same conformer (ID 6) reconstructed by AlphaCyo4D (**d**), PCA in CryoSPARC (**e**) and ML3D in RELION (**f**). The maps are colored by their local resolutions calculated by Bsoft blocres program. **g-i**, Closeup side-by-side comparison of the same two secondary structures, including a loop (upper row) and a helix (lower row), in the NACHT domain illustrates considerable improvements in local density quality and resolution by AlphaCryo4D (**g**) as opposed to PCA/CryoSPARC (**h**) and ML3D/RELION (**i**). The locations of the loop and helix in the NLRP3 structure are marked by dashed boxes in panel (**f**). The same ground-truth atomic model of Conformer 6 shown in stick representations is superimposed with the density maps shown in blue mesh representations, all from the same perspective. The atomic model was not further refined against each map for visual validation of the map accuracy.

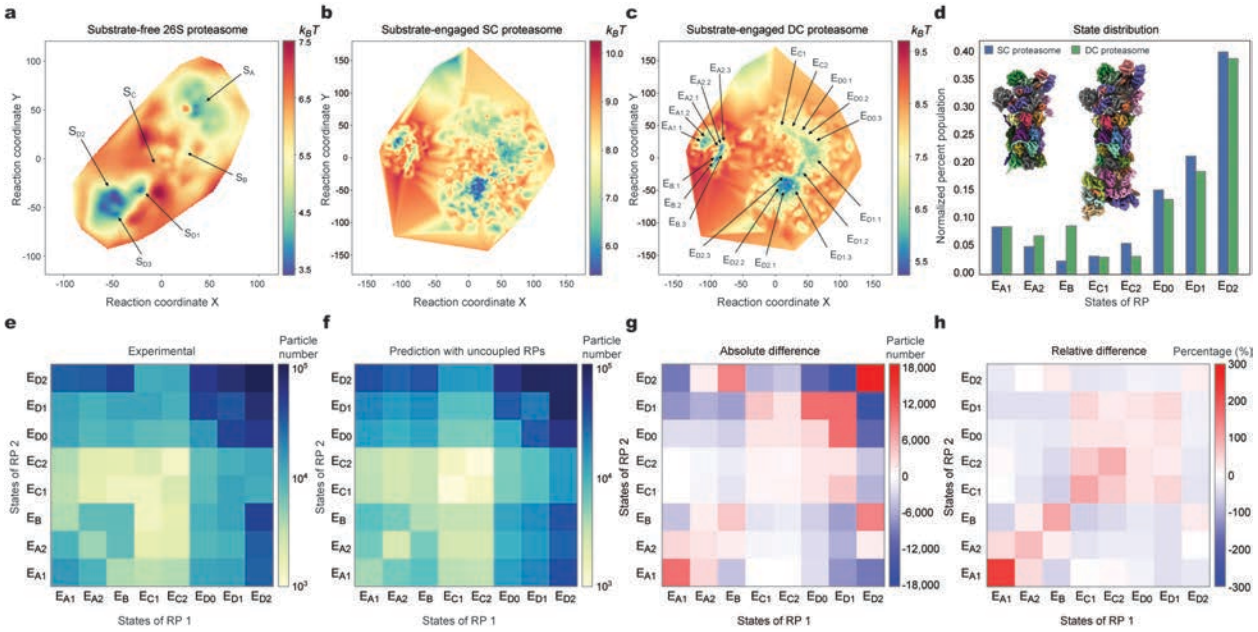

Figure 3. **Energic differences of the singly and doubly capped proteasomes**. **a-c**, Free-energy landscape of the substrate-free ATPγS-bound 26S proteasome (**a**), the substrate-engaged singly capped (SC) proteasome (**b**), and the substrate-engaged doubly capped (DC) proteasomes (**c**) computed by AlphaCryo4D. 19 conformational states of the RP-CP subcomplex are marked on the energy landscape. **d**, Comparison of the state distribution of RP in the SC and DC proteasomes. **e**, State distribution matrix of the DC proteasome obtained using AlphaCryo4D on experimental data, colored by the particle numbers in the DC states, with the horizonal and vertical axes representing the states of two RPs bound to the same CP. **f**, State distribution matrix of the DC proteasome predicted by a control model assuming that the two RPs in the same DC proteasome are completely independent of each other or uncoupled. The model assumes the same total number of DC particles and the same probability of observing each RP state as experimentally measured. **g**, State distribution difference matrix of the DC proteasome by experimental results minus the model predictions assuming uncoupled two RPs, colored by the absolute particle number difference. **h**, Relative differences of the DC proteasome in unit of percentage. The relative difference is the ratio of absolute difference divided by the particle numbers from the model prediction in each DC state.

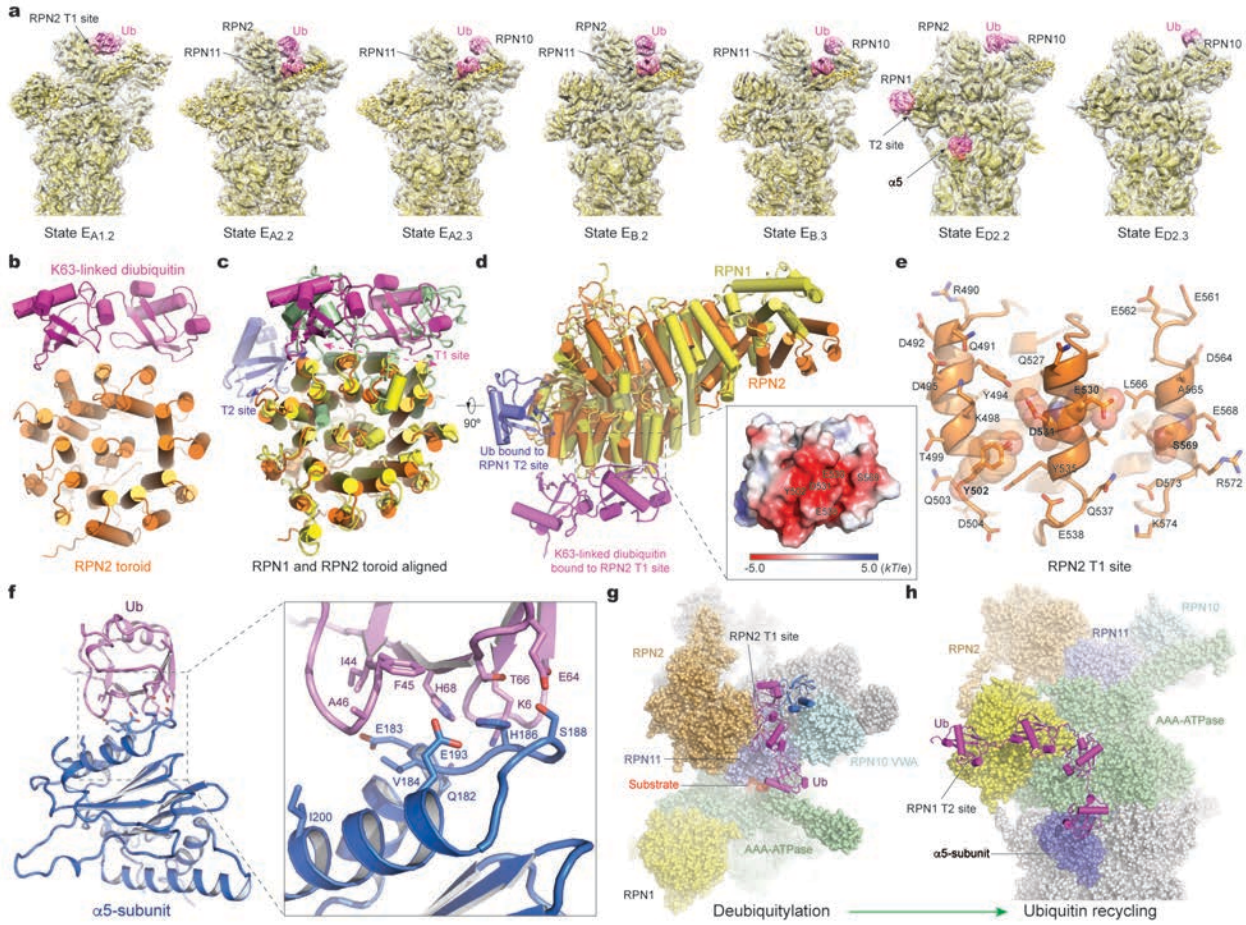

Figure 4. Mapping of novel ubiquitin-binding sites in the 26S proteasome. **a**, Seven lowly populated transient states visualize various ubiquitin-binding sites on the RPN1 T2 site[12], the RPN2 T1 site, the RPN10 VWA site and the α5-subunit site, in addition to the RPN11 deubiquitylation site and previously observed RPT5 coiled-coil site[2]. For clarity of illustrating moderate-resolution ubiquitin (Ub) features, the cryo-EM maps of these states are low-pass filtered at 8 Å and shown in transparent surface representations superimposed with their corresponding atomic models in cartoon representations. The Ub densities are colored magenta, with the rest of the structures colored yellow. **b**, Structure of the RPN2 toroidal domain (orange) in complex with Lys63-linked diubiquitin (magenta) modelled from the cryo-EM maps of states $E_{A1.2}$, $E_{A2.2}$ and $E_{B.2}$, in cartoon representation. **c**, Structure-based alignment of the human RPN1 and RPN2 toroidal domains shown in color yellow and orange, respectively. The RPN1 T2 site-bound ubiquitin is shown as light blue. The NMR structure (PDB ID 2N3V) of the Lys48-linked dibuiquitin-bound yeast Rpn1 T1 site segment[12], shown as light green, is aligned with the human RPN1 structure and is superimposed for comparison. **d**, The entire human RPN1 and RPN2

602 subunit structures are aligned together and viewed from a perspective that is rotated 90° relative
603 to the orientation in panel (**c**), showing that the two subunits are structurally homologous. Insert,
604 electrostatic surface of the RPN2 T1 site showing its acidic nature. **e**, Closeup view of the RPN2
605 T1 site composed of three helices in carton representation with the side chains shown in stick
606 representation. The key residues contacting ubiquitin are highlighted with transparent sphere
607 representation. **f**, Structure of ubiquitin-bound α5 subunit shown in cartoon representation. The
608 side chains of residues involved in the intermolecular interactions are shown in stick
609 representation and are zoomed in on the right. **g**, A Lys63-linked triubiquitin chain model fitted
610 from the cryo-EM maps of states $E_{A2.2}$ and $E_{B.2}$ is shown in purple cartoon representation and
611 spans from the RPN2 T1 site to the RPN11 deubiquitylation site. The RPN10 VWA-bound
612 monoubiquitin fitted in states $E_{A2.3}$ and $E_{B.3}$ is superimposed in blue cartoon representation. The
613 proteasome is shown as space-filling sphere representations. **h**, A Lys63-linked tetraubiquitin
614 chain model derived from the cryo-EM map of state $E_{D2.2}$. The two terminal ubiquitin molecules
615 are fitted from their highest-resolution cryo-EM densities available at the RPN1 T2 and α5-
616 subunit sites, whereas the middle two molecules are hypothetically modelled.

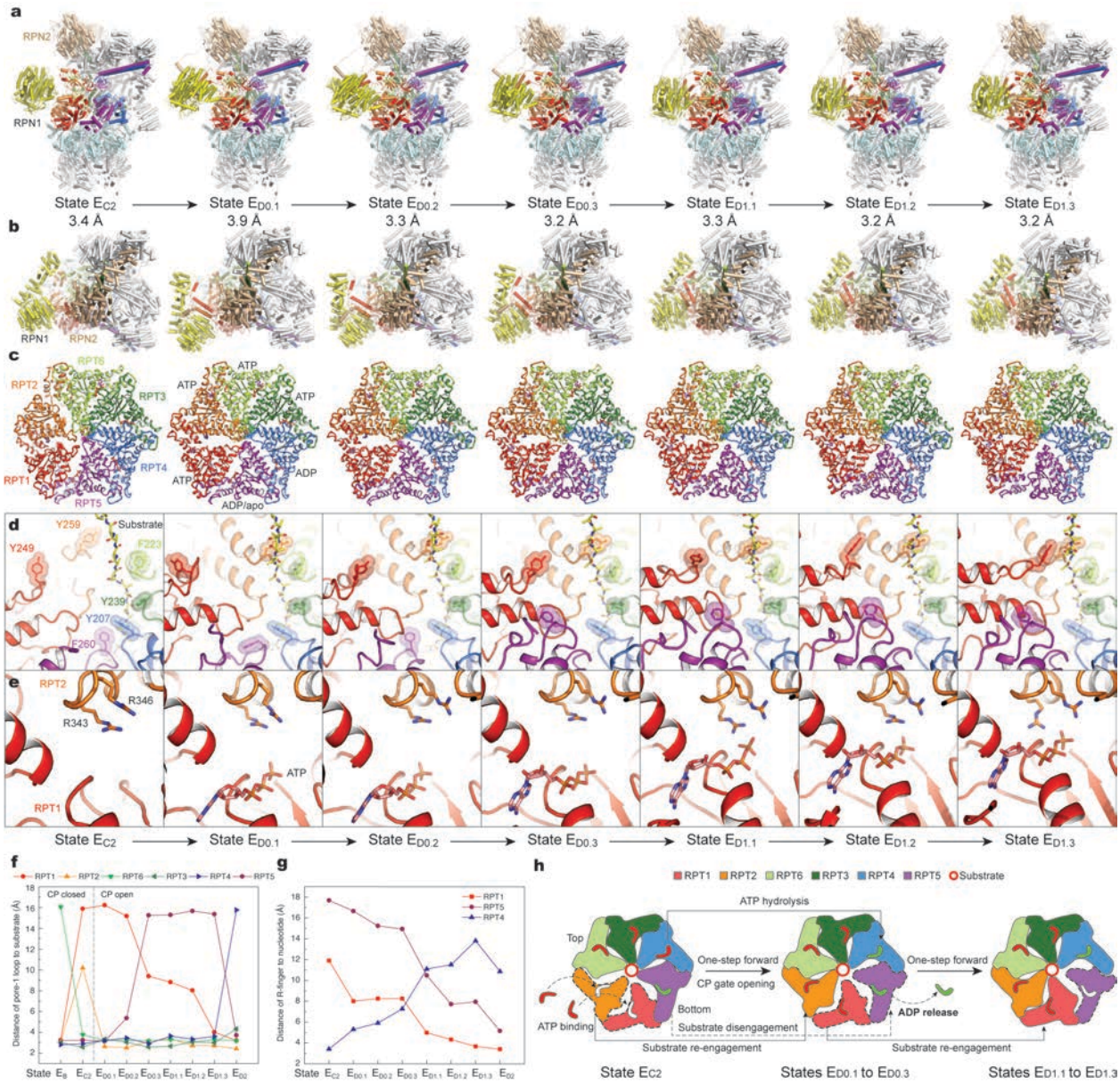

Figure 5. Single-nucleotide exchange dynamics of the AAA-ATPase motor. **a**, Side views of the substate-engaged RP-CP subcomplex in seven sequential conformers between states E_{C2} and $E_{D1.3}$, as shown in cartoon representation and with only half CP shown. **b**, Top views of the seven sequential conformers, showing the overall lid rotation and the relative rotation between RPN1 and the rest of the RP structure. **c**, The substrate-bound AAA-ATPase structures of the seven conformers in cartoon representations. The substrates and nucleotides are shown in stick representations. **d**, Close-up views of the pore-1 loop interactions with the substrate (in yellow stick representation), with the aromatic residues in the pore-1 loops highlighted by transparent sphere representations. The seven snapshots show that the RPT1 pore-1 loop is gradually moved

627 to a position in direct contact with the substrate, whereas the RPT5 pore-1 loop is gradually
628 moved away from the substrate and flipped up and out. **e**, Close-up views of the RPT1
629 nucleotide-binding sites in different states, showing its gradual closeup by the R-fingers from
630 RPT2. **f**, Plots of distances of the pore-1 loops of all RPT subunits to the substrate measured in
631 the atomic structures of 9 sequential conformational states. **g**, Plots of distances of R-finger to
632 the nucleotides bound to three RPT subunits measured in the atomic structures of 8 sequential
633 conformational states. **h**, Schematic illustrating the ATP hydrolysis reaction and nucleotide
634 exchange associated with the intermediates during the transition from state E_{C2} to $E_{D1.3}$.
635
636

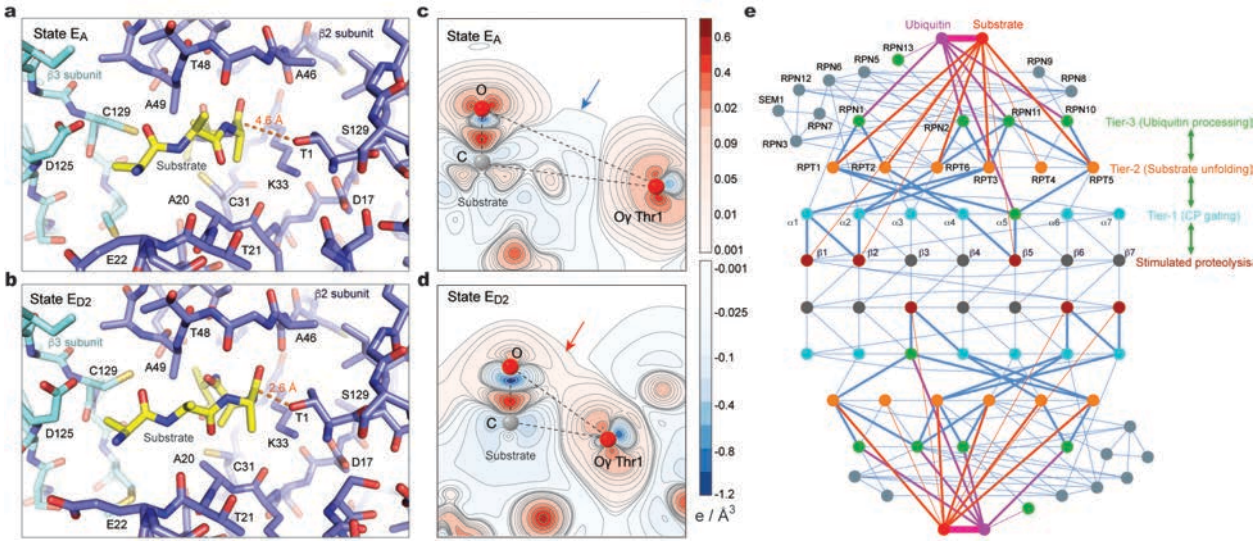

Figure 6. **Hierarchical allosteric regulation of proteasome activity**. **a** and **b**, Structure of the catalytic site with a substrate polypeptide bound at residue Thr1 in the β2 subunit of the CP in the closed-gate state E_A at 2.7-Å resolution (**a**) and in the open-gate state E_{D2} at 2.5-Å resolution (**b**). **c** and **d**, Charge density difference contour maps at the proteolytic active site of the β2 subunit computed by the quantum mechanical DFT based on the atomic structures of states E_A (**c**) and E_{D2} (**d**). The contours are plotted in the plane passing through the Thr1-Oγ atom and the nearest carbonyl carbon and oxygen atoms of the substrate. The interactions of the Thr1-Oγ atom and the carbonyl group lead to the nucleophilic attack as the first step of the proteolytic process. Due to the proximity shown in (**b**), a bonding interaction starts to form in the E_{D2} states, indicated by the slight positive charge difference region (red arrow), whereas there is no such region formed in the E_A state and the pair is well separated by a non-bonding charge depletion region (blue arrow). **e**, An interactome network diagram of the proteasome illustrating the grand allosteric regulation model and highlighting the key inter-subunit interaction pathways for proteasome autoregulation. The base subunits hosting ubiquitin-binding sites and the deubiquitinase RPN11 are shown as the green nodes; the AAA-ATPase subunits as the orange nodes; the α-type subunits as the cyan nodes; the catalytically active β1, β2 and β5 subunits as the crimson nodes. Steal blue lines represent inter-subunit interactions; purple lines represent the interactions with ubiquitin; and red lines represent substrate polypeptide interactions. Bold lines highlight the shortest pathways connecting the three tiers of regulatory subunits that are expected to propagate the allosteric regulation from ubiquitin interactions down to the six proteolytic

658 active sites in the CP. The network diagram is constructed according to all 64 structural models
659 of the substrate-bound proteasome in this study.
660

Methods

Overall procedure of AlpahCryo4D

The design of AlphaCryo4D follows a few key ideas and objectives. First of all, we expect to maximally use all available particles and make particle selection via comprehensive, objective criteria such as the reproducibility and robustness in deep-learning-based classification. To this end, we minimize any substantial manual particle rejection before entering the steps of AlphaCryo4D and avoid any subjective particle selection within the AlphaCryo4D procedure. Next, we expect to devise an automated procedure to examine the robustness of 3D classification at single-particle level. We consider that any objective functions in image similarity measurement suffer from certain degree of errors in particle alignment that often lead to a greater degree of misalignment with decreasing the signal-to-noise ratio (SNR). Thus, we expect to devise an integrative procedure in which each particle is analyzed for at least three times to examine the robustness of the 3D classification algorithm with respect to individual particles. We wish to keep particle images that exhibits greater robustness during data processing. Thus, within the entire AlphaCryo4D procedure, the only way to reject particles is via the energy-based particle voting algorithm that is completely objective.

In practice, AlphaCryo4D consists of four major steps (Fig. 1a). First, all single-particle images are randomly divided into M+1 groups of equal data sizes. In the step called 'particle shuffling', one group of particles is taken out of the dataset to form a shuffled dataset. This procedure is repeated for $M + 1$ times, each time with a different particle group being taken out, resulting in $M + 1$ shuffled datasets (Extended Data Fig. 1). Each shuffled dataset is subject to 3D volume bootstrapping separately. In each case, all particles in a shuffled dataset are aligned in a common frame of reference through a consensus 3D refinement, and then clustered into tens to hundreds of 3D reconstructions through Bayesian clustering, which ensures that only structurally similar particles are clustered into the same 3D volumes. In total, thousands of volumes from all shuffled datasets are expected to be bootstrapped through these steps. As a result, each particle image is used in 3D reconstructions of M different volumes after particle shuffling and volume bootstrapping. Second, all bootstrapped volumes are learnt by an autoencoder based on a deep residual convolutional neural network in an unsupervised fashion[3,20] (Fig. 1b, Extended Data Table 1). A 3D feature map is extracted for each volume and is juxtaposed with the volume data for nonlinear dimensionality reduction by manifold

692 embedding with t-distributed stochastic neighbor embedding (t-SNE) algorithm[4]. Third, the
693 learnt manifold is then used to compute a free-energy landscape via the Boltzmann distribution[5].
694 A string method is used to search the minimum energy path (MEP) on the learnt free-energy
695 landscape[21,22]. The local energy minima or the transition states connecting can be defined as the
696 centers of 3D clustering, with a circular range defined as cluster boundaries for subsequent
697 particle voting. Forth, because each particle is used *M* times during volume bootstrapping, it is
698 mapped to *M* locations on the free-energy landscape. The mapping of each copy of the particle is
699 called a 'vote'. By counting the number of votes of the same particle being mapped within the
700 same cluster boundary on the energy landscape, we can evaluate the reproducibility of manifold
701 learning at single-particle level. Each particle is classified to the 3D cluster that receives more
702 than $M/2$ votes of this particle. If none of the 3D clusters on the energy landscape receives more
703 than $M/2$ votes of a given particle, the corresponding particle is voted out in the procedure and is
704 excluded for further 3D reconstruction. As a result, each of the final 3D reconstructions includes
705 structurally homogeneous particles that can potentially achieve higher resolution.
706 AlphaCryo4D exhibits several advantages as well as certain limitation. First, it allows a
707 maximal number of particles to be assessed and classified in an integrative procedure based on
708 uniform, objective criteria, such as their reproducibility and robustness in deep learning. Second,
709 the energy-based particle-voting algorithm can potentially rescue certain particles that are prone
710 to be misclassified if processed only once, thus boosting the efficiency of particle usage without
711 necessarily sacrificing quality and homogeneity of selected particles. Third, the use of energy
712 landscape to direct 3D clustering of conformational states has an intuitive physical meaning and
713 allows users to examine kinetic relationships between the adjacent states at the same time of
714 conducting 3D classification and to potentially discover new conformations. All these
715 advantages are well demonstrated in our analysis of both simulated and experimental datasets.
716 The limitation of AlphaCryo4D lies in that it requires generally larger datasets and more
717 computational costs to fully exploit its advantages. We do not expect to achieve considerably
718 better results for a small dataset. Moreover, its outcomes are dependent on the success of initial
719 consensus alignment of all particles during the first step of particle shuffling and volume
720 bootstrapping. Failure in obtaining accurate alignment parameters can lead to futile, erroneous,
721 nonsensical classification in the subsequent steps.
722 **Particle shuffling for bootstrapping 3D volumes**

723 A key philosophy of the AlphaCryo4D design is to avoid subjective judgement on the particle
724 quality and usability as long as it is not apparent junks like ice contaminants, carbon edge and
725 other obvious impurities. A deep-learning-based particle picking in DeepEM[44], Torpaz[45] or other
726 similarly performed software is favored for data preprocessing prior to AlphaCryo4D. To
727 prepare particle datasets for AlphaCryo4D, an initial unsupervised 2D image classification and
728 particle selection, preferentially conducted by the statistical manifold-learning-based algorithm
729 in ROME[17], is necessary to ensure that no apparent junks are selected for further analysis and
730 that the data have been collected under an optimal microscope alignment condition, such as
731 optimized coma-free alignment. No particles should be discarded based on their structural
732 appearance during this step if they are not apparent junks. Any additional 3D classification
733 should be avoided to pre-maturely reject particles prior to particle shuffling and volume
734 bootstrapping in the first step of AlphaCryo4D processing. Pre-maturely rejecting true particles
735 via any 2D and 3D classification is expected to introduce subjective bias and to impair the native
736 conformational continuity and statistical integrity intrinsically existing in the dataset.
737 In raw cryo-EM data, 2D transmission images of biological macromolecules suffer from
738 extremely heavy background noise, due to the use of low electron dose to avoid radiation
739 damage. To tackle the conformational heterogeneity of the protein sample of interest in the
740 presence of heavy image noise, we devised the particle shuffling and volume bootstrapping
741 procedure that incorporates the Bayesian or maximum-likelihood-based 3D clustering[8]. To
742 enable the particle-voting algorithm in the late stage of AlphaCryo4D, each particle is reused M
743 times during particle shuffling to bootstrap a large number of 3D volumes (Extended Data Fig.
744 1a). First, all particle images are aligned to the same frame of reference in a consensus 3D
745 reconstruction and refinement in RELION[8] or ROME to obtain the initial alignment parameters
746 of three Euler angles and two translational shifts. Optimization for high alignment accuracy in
747 this step must be pursued to make the volume bootstrapping more efficient and to avoid the error
748 propagation to the subsequent steps in AlphaCryo4D. Thus, coarsely classifying the dataset
749 during image alignment, restricting the 3D alignment to a moderate resolution like 10 Å or 15 Å
750 for global parameter search, progressing to small enough angular steps in the final stage of
751 consensus refinement, must be appropriately practiced in order to optimize the initial 3D
752 alignment of all particles. Failure of initial alignment of particles would lead to failure of all
753 subsequent AlphaCryo4D analysis.

754 Next, based on the results of consensus alignment, in the particle-shuffling step, all particles
755 were divided into $M + 1$ groups, and M was set to an odd number of at least 3. Then the whole
756 dataset was shuffled $M + 1$ times by removing a different group out of the dataset each time.
757 Each shuffled dataset is classified into a large number of 3D volumes, often several hundreds, by
758 the maximum-likelihood classification algorithm without further image alignment in RELION.
759 This step is repeated $M + 1$ times, each time on a shuffled dataset missing a different group
760 among the $M + 1$ groups. Due to the effect of M-fold data augmentation and enhancement by
761 particle shuffling, the outcome of this entire process is expected to bootstrap up to thousands of
762 3D volumes in total. Each particle is used and contributed to the 3D reconstructions of M
763 volumes, which prepare it for the particle-voting algorithm to evaluate the robustness and
764 reproducibility of each particle with respect to the deep learning-based 3D classification later.
765 For processing a large dataset including millions of single-particle images, it becomes
766 infeasible even for a modern high-performance computing system to do the consensus alignment
767 by including all particles once in a single run due to limitation of supercomputer memory and the
768 scalability of the alignment software such as RELION or ROME, although ROME has been
769 specifically optimized for its scalability on CPU-based supercomputing cluster[17] and RELION
770 has been optimized for GPU-based cluster[9]. To tackle this issue, the whole dataset is randomly
771 split into a number of sub-datasets for batch processing, with each sub-dataset including about
772 one to two hundred thousand particles, depending on the scale of available supercomputing
773 system. This strategy can substantially reduce the supercomputer memory pressure and
774 requirement. In each sub-dataset, all particles were divided into $M + 1$ groups and subject to the
775 particle shuffling and volume bootstrapping procedure as described above. To balance the
776 computational cost and algorithmic efficiency, we used $M = 3$ in the entire data processing
777 workflow involved in the current study, implying that every particle was used three times for
778 subsequent computation before particle voting. But a higher M value might be beneficial for
779 smaller dataset or lower signal-to-noise ratio, whose effects are not investigated in the present
780 study due to the limit of computational resources and feasibility.

781 **Deep residual autoencoder for 3D feature extraction**

782 To extract the deep 3D features of the bootstrapped volume data in an unsupervised manner, a
783 3D autoencoder was constructed using a deep Fully Convolutional Network (FCN) composed of
784 residual blocks[3,20]. The structure of the 3D autoencoder consists of the encoder and the decoder,

which are denoted as $\mathcal{E}$ and $\mathcal{D}$, respectively (Fig. 1b, Extended Data Table 1). The relation between the output $\boldsymbol{y}$ and the input $\boldsymbol{x}$ of the network can be expressed as:

$$\boldsymbol{y} = \mathcal{D}\big(\mathcal{E}(\boldsymbol{x})\big), \quad (1)$$

in which $\boldsymbol{x}$ is the input 3D density volume with the size of N^3, where N is the box size of the density map in a unit of pixels. For reconstruction of the 3D volumes and further optimization, the decoding output $\boldsymbol{y}$ should be in the same size and range with the input data $\boldsymbol{x}$. In this way, the framework of FCN is established to restore the input volume, using the sigmoid function $S(x) = \frac{1}{1+\exp(-x)}$ as the activation function of the decoding layer to normalize the value of $\boldsymbol{y}$ into the range (0, 1). Meanwhile, all 3D density maps $\boldsymbol{x}$ should be preprocessed as the function (2) before inputted to the deep neural network:

$$x_{ijk} := \frac{x_{ijk} - x_{min}}{x_{max} - x_{min}}, \quad i, j, k = 1,2, \dots, N. \quad (2)$$

where x_{min} and x_{max} are, respectively, the minimum and minimax value in all x_{ijk}.

The distance between the decoded maps and the input volumes can be used for constructing the loss function to train the 3D kernels and bias of the networks. The value distribution of the encoded 3D feature maps $\boldsymbol{z} = \mathcal{E}(\boldsymbol{x})$ is expected to be an abstract, numerical representation of the underlying structures in the volume data, which may not necessarily have any intuitive real-space physical meanings. The neural network is capable of extracting such abstract information in the prediction step, with no restriction on the feature maps $\boldsymbol{z}$ in the expression of training loss. The loss function is then formulated as:

$$L(\boldsymbol{\theta}; \boldsymbol{x}, \boldsymbol{y}) = \frac{1}{N^3} \sum_{i,j,k=1}^{N} \left\| x_{ijk} - y_{ijk} \right\|^2 + \lambda \|\boldsymbol{\theta}\|^2, \quad (3)$$

where $\boldsymbol{\theta}$ denotes the weights and bias of the network, and λ is L2 norm regularization coefficient. As the feature of the complex structure is difficult to be learnt from the 3D volume data, the value of λ is generally set to 0 to focus on the first term of the expression (3) unless overfitting arises.

To improve the learning capacity of the 3D autoencoder, residual learning blocks containing 3D convolution and transpose convolution layers are employed in the encoder and decoder, respectively. In each residual block, a convolution/transpose convolution layer followed by Batch Normalization (BN) layer and activation layer appears twice as a basic mapping, then

adding with the input to generate the output. The mathematical expression of the lth block can be shown as:

$$\begin{cases} \boldsymbol{y_l} = \mathcal{F}(\boldsymbol{x_l}; \boldsymbol{\theta}_l) + \boldsymbol{x_l} \\ \mathcal{F}(\boldsymbol{x_l}; \boldsymbol{\theta}_l) = \mathcal{C}\big(\mathcal{C}(\boldsymbol{x_l})\big), \\ \mathcal{C}(\boldsymbol{x_l}) = a(b(c(\boldsymbol{x_l}))) \end{cases} \quad (4)$$

where $\boldsymbol{x_l}$ and $\boldsymbol{y_l}$ represent the input and the output of this block, respectively. $\mathcal{F}(x_l; \boldsymbol{\theta}_l)$ denotes the basic mapping of the lth block parameterized by $\boldsymbol{\theta}_l$, and $\mathcal{C}(\boldsymbol{x_l})$ is the sequential operation of convolution/transpose convolution c, BN b and activation a. The rectified linear unit (ReLU) function is used in all the activation layers but the last one. In addition, the function (4) demands that the output of mapping function $\mathcal{F}(\boldsymbol{x_l}; \boldsymbol{\theta}_l)$ must have the same dimension as the input $\boldsymbol{x_l}$. If this is not the case, the input $\boldsymbol{x_l}$ must be rescaled along with $\mathcal{F}(\boldsymbol{x_l}; \boldsymbol{\theta}_l)$ using a convolution/transpose convolution transformation $c'(\boldsymbol{x_l})$ with an appropriate stride value, the parameters of which can be updated in the training step.

To analyze a large number of volumes, training of the autoencoder neural network should be treated elaborately to obtain suitable kernels and bias. First of all, parallel computation with multiple GPUs must be implemented to reduce the training time. Then the parameters of the network are optimized by the stochastic gradient descent Adam (Adaptive moment estimation) algorithm, in which the gradients of the objective function $L(\boldsymbol{\theta}; \boldsymbol{x}, \boldsymbol{y})$ with respect to the parameters $\boldsymbol{\theta}$ can be calculated by the chain rule. Moreover, the learning rate will be reduced to one tenth if the loss function does not decrease in three epochs based on the initial value of 0.01. After trained about 50 epochs, the best model is picked to execute the task of structural feature extraction. Using the unsupervised 3D autoencoder, the feature maps $\boldsymbol{z} = \mathcal{E}(\boldsymbol{x})$ encoding the structural discrepancy among the 3D volume data can be extracted automatically without any human intervention.

Manifold embedding of free energy landscape

To prepare for the energy landscape reconstitution, each bootstrapped 3D volume was juxtaposed with its 3D feature map learnt by the autoencoder to form an expanded higher-dimensional data point. All the expanded data points were then embedded onto a low-dimensional manifold via the t-SNE algorithm by preserving the geodesic relationships among all high-dimensional data[4]. During manifold embedding, it is assumed that the pairwise similarities in the high dimensional data space and low dimensional latent space follow a

Gaussian distribution and a Student's t-distribution, respectively, which can be formulated as:

$$\begin{cases} p_{ij} = \dfrac{\exp\left(-\left\|\boldsymbol{x}_i - \boldsymbol{x}_j\right\|^2 / 2{\sigma_i}^2\right)}{\sum_{i \neq j} \exp\left(-\left\|\boldsymbol{x}_i - \boldsymbol{x}_j\right\|^2 / 2{\sigma_i}^2\right)}, \quad i \neq j \\ q_{ij} = \dfrac{\left(1 + \left\|\boldsymbol{y}_i - \boldsymbol{y}_j\right\|^2\right)^{-1}}{\sum_{i \neq j}\left(1 + \left\|\boldsymbol{y}_i - \boldsymbol{y}_j\right\|^2\right)^{-1}}, \quad i \neq j \end{cases} \quad (5)$$

where p_{ij} and q_{ij} represent the similarity distributions in the high and low dimensional spaces, $\boldsymbol{x}_k$ and $\boldsymbol{y}_k$ $(k = i, j)$ are the data points of the high and low dimensional spaces, respectively. The parameter σ^2 is the variance of the Gaussian distribution. In addition, p_{ii} and q_{ii} are both set to zero to satisfy the constraint of symmetry.

To find the value y_k of each data point, an objective function measuring the distance between the similarity distribution p_{ij} and q_{ij} had to be well defined. Here the relative entropy, also called the Kullback-Leibler (KL) divergence,

$$KL(P \parallel Q) = \sum_{i,j} p_{ij} \log \frac{p_{ij}}{q_{ij}}, \quad (6)$$

was employed and minimized by the gradient descent algorithm with the momentum method[46].

After the manifold embedding by t-SNR, each 3D volume is mapped to a low-dimensional data point in the learnt manifold. The coordinate system, in which the low-dimensional representation of the learnt manifold is embedded, is used for reconstructing and visualizing the free energy landscape. In accordance with the Boltzmann distribution, the free energy of each data point in the low-dimensional space can be estimated using the particle number included in the original 3D volume corresponding to each low-dimensional data point on the manifold:

$$\Delta\Delta G_i = -k_B T \ln \frac{N_i}{\sum_i N_i}, \quad (7)$$

where $\Delta\Delta G_i$ denotes the free energy difference of the data point with the particle number of N_i against a common reference energy level, k_B is the Boltzmann constant and T is the temperature in Kelvin. The free energy landscape was plotted by interpolation of the free energy difference in areas with sparse data.

Minimum energy path finding using the string method

The string method is an effective algorithm to find the minimum energy path (MEP) on the potential energy surface[21]. To extract the dynamic information implicated in the experimental free energy landscape, an improved and simplified version of the string method was developed to

search the possible state-transition pathway or MEP[22]. Along the MEP on the learnt energy landscape, the local minima of interest could be defined as 3D clustering centers to guide the particle-voting algorithm for 3D classification, on the basis of which particles of the same conformation could be clustered to generate high-resolution cryo-EM density maps (Extended Data Fig. 1b). The objective of the MEP identification in barrier-crossing events lies in finding a curve γ having the same tangent direction as the gradient of free energy surface ∇G. It can be expressed as:

$$(\nabla G)^{\perp}(\gamma) = 0, \quad (8)$$

where $(\nabla G)^{\perp}$ denotes the component of ∇G perpendicular to the path γ. To approach the objective function (4), two computational steps, named evolution of the images and reparameterization of the string, are iterated until convergence within a given precision threshold.

Evolution of the images. After initialization with the starting and ending points, the positions of interval images were updated according to gradient of the free energy at the tth iteration:

$$\varphi_i^{*(t)} = \varphi_i^{(t-1)} - h\nabla G\left(\varphi_i^{(t-1)}\right), \quad (9)$$

with $\varphi_i^{(t)}$ $(i = 0,1,\dots,N)$ being the ith intermediate image at the tth iteration ($*$ denoting the temporary values), and h the learning rate.

Reparameterization of the string. The values of positions $\varphi_i^{(t)}$ $(i = 0,1,\dots,N)$ were interpolated onto a uniform mesh with the constant number of points. Prior to interpolation, the normalized length $\alpha_i^{*(t)}$ $(i = 0,1,\dots,N)$ along the path was calculated as:

$$\alpha_0^{*(t)} = 0, \quad \alpha_i^{*(t)} = \alpha_{i-1}^{*(t)} + \frac{\left\|\varphi_i^{*(t)} - \varphi_{i-1}^{*(t)}\right\|}{\sum_{i=1}^{N}\left\|\varphi_i^{*(t)} - \varphi_{i-1}^{*(t)}\right\|}, \quad i = 1,2,\dots,N. \quad (10)$$

Given a set of data points $(\alpha_i^{*(t)}, \varphi_i^{*(t)})$, the linear interpolation function was next used to generate the new values of positions $\varphi_i^{(t)}$ $(i = 0,1,\dots,N)$ at the uniform grid points $\alpha_i^{(t)}$ $(i = 0,1,\dots,N)$. The iteration was terminated when the relative difference $\sum_{i=0}^{N}\left\|\varphi_i^{(t)} - \varphi_i^{(t-1)}\right\|^2/N$ became small enough.

Energy-based particle voting algorithm

The particle-voting algorithm was designed to conduct 3D classification, particle quality control, reproducibility test and particle selection in an integrative manner. The particle-voting algorithm

896 mainly involves two steps (Extended Data Fig. 1b). First, we count the number of votes for each
897 particle mapped within the voting boundaries of all 3D clusters on the free-energy landscape.
898 One vote is rigorously mapped to one copy of the particle used in reconstructing a 3D volume
899 and to no more than one 3D cluster on the energy landscape where the corresponding volume is
900 located. Thus, each particle can have M votes casted for no more than M 3D clusters. If the vote
901 is mapped outside of any 3D cluster boundary, it becomes an 'empty vote' with no cluster label.
902 Each non-empty vote is thus labeled for both its particle identify and corresponding cluster
903 identify. For each pair of particle and cluster, we compute the total number (K) of votes that the
904 cluster receives from the same particle. Each particle is then assigned and classified to the 3D
905 cluster that receives $K > M/2$ votes from this particle (Extended Data Fig. 1b). Note that after
906 particle voting, each particle is assigned no more than once to a 3D class, with its redundant
907 particle copies removed from this class. This strategy only retains the particles that can
908 reproducibly vote for a 3D cluster corresponding to a homogeneous conformation, while
909 abandoning those non-reproducible particles with divergent, inconsistent votes.
910 Because the particle-voting algorithm imposes strong constraints on the numeric performance
911 of particles in deep learning, it could lead to particle number insufficiency in the cases of smaller
912 but potentially interested 3D classes. To remedy this limitation, an alternative, distance-based
913 classification algorithm was devised to replace the particle-voting algorithm when there are not
914 enough particles to gain the advantage of particle voting (Extended Data Fig. 1c). In this method,
915 the distances of all M copies of each particle to all 3D cluster centers on the energy landscape are
916 measured and ranked. Then, the particle is classified to the 3D cluster of the shortest distance. A
917 threshold could also be manually preset to remove particles that are too far away from any of the
918 cluster centers. The distance-based classification method can keep more particles, but it ignores
919 the potential issue of irreproducibility of low-quality particles. Thus, it is proven to be less
920 accurate in 3D classification (Extended Data Fig. 5d, i, n). In other words, it trades off the
921 classification accuracy and class homogeneity to gain more particles, which is expected to be
922 potentially useful for small datasets or small classes. By contrast, the energy-based particle-
923 voting algorithm imposes a more stringent constraint to select particles of high reproducibility
924 during classification, resulting in higher quality and homogeneity in the classified particles,
925 which is superior to the distance-based classification method (Extended Data Fig. 5e, j, o).
926 **Data-processing workflow of AlphaCryo4D**

Input: single-particle cryo-EM dataset after initial particle rejection of apparent junks.

Output: free energy landscape, MEP, 3D class assignment of each particle and high-resolution density maps.

1. Bootstrap a large number of 3D volumes through particle shuffling, consensus alignment and Bayesian classification.
    a. Split the particles dataset randomly to many sub-datasets, if necessary, for batch processing of particle shuffling and volume bootstrapping.
    b. For each sub-dataset, conduct consensus alignment to generate initial parameters of Euler angles and translations.
    c. Divide each sub-dataset into $M + 1$ groups, shuffle the sub-dataset $M + 1$ times and each time take a different group out of the shuffled sub-dataset, giving rise to $M + 1$ shuffled sub-datasets all with different collection of particles.
    d. Conduct 3D Bayesian classification on all the $M + 1$ shuffled sub-datasets to generate hundreds of 3D volumes, making each particle to contribute to M different volumes.
    e. Repeat steps (b) to (d) for all sub-datasets.
2. Extract deep features of all volume data with the 3D deep residual autoencoder.
    a. Initialize the hyper-parameters of the 3D autoencoder in Table 1.
    b. Train this neural network with the 3D volume data to minimize mean square error between the decoding layer and the input by the Adam algorithm of initial learning rate 0.01.
    c. Extract the feature maps of all volumes from the encoding layer.
3. Embed the volume data to low-dimensional manifolds through the t-SNE algorithm and compute the free-energy landscape.
    a. Calculate the pairwise similarities between volumes using their feature-map-expanded volume vectors, and randomly initialize the low-dimensional points.
    b. Minimize the KL divergence by the Momentum algorithm to generate the low-dimensional embeddings.
    c. Compute the free energy landscape with the low-dimensional coordinates.
4. Apply the string method to find the MEP on the free energy landscape, along which 3D density maps of the same conformation are clustered together.

958 a. Initialize the transition path with a straight line between the given starting and
959 ending points.
960 b. Update the transition path according to Equations (9) and (10) until it converges
961 to the expected MEP.
962 c. Sample the clustering centers along the MEP and calculate the recommended
963 clustering radius.
964 5. Classify all particles through the energy-based particle-voting algorithm.
965 a. Define the local energy minima as the 3D clustering centers and their
966 corresponding cluster boundary for particle voting.
967 b. For each particle, cast a labelled vote for a 3D cluster when a volume containing
968 one of the *M* particle copies is located in the voting boundary of the 3D cluster.
969 c. Count the number of votes of each particle with respect to each 3D cluster and
970 assign the particle to the 3D cluster that receives more than *M*/2 votes from this
971 particle.
972 6. Refine the 3D density maps to high resolution using particles classified into the same 3D
973 classes.
974 **Blind assessments using simulated datasets**
975 Three simulated datasets with the SNRs of 0.05, 0.01 and 0.005 were employed to benchmark
976 AlphaCryo4D and to compare its performance with conventional methods. Particles were
977 computationally simulated by projecting the 20 3D density maps calculated from 20 hypothetical
978 atomic models emulating continuous rotation of the NLRP3 inflammasome protein. The 20
979 atomic models were interpolated between the inactive NLRP3 structure and its hypothetical
980 active state, which was generated through homology modeling using the activated NLRC4
981 structure[23]. The 20 atomic models represent sequential intermediate conformations during a
982 continuous rotation in its NATCH domain against its LRR domain over an angular range of 90°.
983 Each conformation is thus rotated 4.5° over its immediate predecessor in the conformational
984 continuum sequence. 100,000 simulated particle images per conformational state were generated
985 with random defocus values in range of -0.5 to -3.0 μm, resulting in 2 million particles for each
986 dataset of a given SNR. The pixel size of the simulated image was set to the same as the pixel
987 size (0.84 Å) of the real experimental dataset of NLRP3-NEK7 complex. To emulate realistic
988 circumstances in cryo-EM imaging, Gaussian noises, random Euler angles covering half a sphere

989 and random in-plane translational shifts from -5.0 to 5.0 pixels were then added to every particle
990 image.
991 Each of the three simulated heterogeneous NLRP3 datasets of three different SNRs were
992 analyzed separately by AlphaCryo4D and used to characterize the performance and robustness of
993 AlphaCryo4D against the variation of SNR. In the step of particle shuffling and volume
994 bootstrapping, 2,000,000 particles in the dataset of any given SNR were divided randomly into
995 10 sub-datasets for batch processing. The orientation of each particle was determined in the
996 initial 3D consensus alignment in RELION, which did not change in the subsequent 3D
997 classification. In this step, the maximum number of iterations of the 3D alignment was set up as
998 30, with the initial reference low-pass filtered to 60 Å. 3-fold particle shuffling (indicated as × 3
999 below) was conducted on each sub-dataset for volume bootstrapping. The first round of
1000 maximum-likelihood 3D classification divided the input shuffled particle sub-dataset into 5
1001 classes, each of these classes were then further classified into 8 classes. This procedure was
1002 repeated on all shuffled particle sub-datasets. The particle shuffling and volume bootstrapping
1003 generated 1,372, 1,489, and 1,587 volumes by the datasets with SNRs of 0.05, 0.01 and 0.005,
1004 respectively. These volume data were used as inputs for deep residual autoencoder to compute
1005 low-dimensional manifolds and free-energy landscapes (Fig. 1d-f, Extended Data Fig. 2a, b).
1006 After searching the MEP on the energy landscapes by the string method, 20 cluster centers along
1007 the MEP were defined by the local energy minimum along the MEP that represent potentially
1008 different conformations of the molecule (Extended Data Fig. 2a-c). The particle-voting algorithm
1009 was applied in every cluster to determine the final particle sets for all 3D classes. For the purpose
1010 of validation of the methodology and investigation of 3D classification improvement, we labeled
1011 each bootstrapped 3D volume with the conformational state that held the maximum proportion of
1012 particles in the class and computed its 3D classification precision as the ratio of the particle
1013 number belonging to the labelled class versus the total particle number in the volume (Fig. 1d,
1014 Extended Data Fig. 2a, b). Moreover, 3D classification precision and its statistical distribution
1015 among the bootstrapped data calculated from the ground truths were recorded in the intermediate
1016 steps of AlphaCryo4D, including the particle shuffling and volume bootstrapping, setup of
1017 voting boundary on the free energy landscape, distance-based 3D clustering and energy-based
1018 particle voting (Extended Data Fig. 5).
1019 To compare the classification performance of AlphaCryo4D with other methods, the ab-initio

classification by 3D PCA analysis in CryoSPARC[7] and the maximum-likelihood-based 3D (ML3D) classification in RELION[8,9,18] had been tested on the simulated datasets. For the tests using RELION, we classified all particles directly into 20 classes and hierarchically into 4 × 5 classes, which first divided the dataset into 4 classes, with each class further classified into five sub-classes (Extended Data Fig. 3). In the 3D PCA analysis using CryoSPARC, we first did the consensus alignment of the entire dataset to find the orientation of each particle. Then the alignment and the mask generated from the consensus alignment were used as inputs into the 3D PCA calculation, with the number of orthogonal principal modes being set to 2 in 3D classification, in consistent with the deep manifold learning algorithm. Then the 3D variability display module in the cluster mode was used to analyze the result of 3D classification. The metadata of 3D classification precisions as well as the 3D density maps from all the algorithms applied on the three simulated datasets were collected to conduct statistical analysis, as shown in Fig. 2 and Extended Data Figs. 2-5.

Computational costs of AlphaCryo4D

Although the computational cost of AlpahCryo4D is generally higher than the conventional approach, it does not appear to increase drastically and likely falls in an affordable range, while reducing the average cost of computation per conformational state. In a nutshell, we can have a brief comparison of the computational efficiency on the simulated dataset with an SNR of 0.01. In the step of 3D data bootstrapping, we split the dataset into 20 subsets, which contained 100,000 particles each. The 3D consensus alignment of all 2,000,000 particles cost about 75 hours using 8 V100 GPUs interconnected with the high-speed NVLink data bridge in a NVIDIA DGX-1 supercomputing system. Within each subset, the 3D Bayesian classification for one leave-one-group-out dataset cost about 2.5 hours using 320 CPUs, so the total time spent in one subset was about 10 hours using 320 CPUs in an Intel processor-based HPC cluster. In addition, it spent about 3 hours to extract feature via deep neural network using 8 V100 GPUs of the NVIDIA DGX-1 system. In contrast to about 160 hours cost in traditional classification methods, this approach cost a little more than 200 hours using 8 V100 GPUs and 320 CPUs. Taken together, these observations suggest that the computational cost and efficiency of AlphaCryo4D are within the acceptable range considering the output of more higher-resolution conformers reconstructed by these procedures.

Applications to experimental cryo-EM datasets

1051 Three experimental cryo-EM datasets were processed using AlphaCryo4D to examine its
1052 applicability in processing real experimental cryo-EM data: (1) A small dataset of the ATPγS-
1053 bound human proteasome[15] contains only 455,680 particles, with the super-resolution pixel size
1054 of 0.685 Å. The size of ATPγS-bound proteasome dataset was enhanced to 455,680 × 3 particles
1055 and was separated into 4 sub-datasets for volume bootstrapping. 160 volumes were bootstrapped
1056 to compute the free-energy landscape the substrate-free ATPγS-bound proteasome (Fig. 3a). (2)
1057 The substrate-engaged human proteasome dataset[2] includes 3,254,352 RP-CP particles (mixed
1058 with particle images from both the DC and SC proteasomes) in total, with the physical pixel size
1059 of 1.37 Å and the box size of 300 pixels. Sample preparation, cryo-EM imaging and data
1060 collection condition as well as data pre-processing prior to 3D classification by AlphaCryo4D
1061 have been previously described in detail[2]. To proceed with AlphaCryo4D, the whole dataset was
1062 randomly split into dozens of sub-datasets, each with 100,000 particles. Particle shuffling and
1063 volume bootstrapping procedures were repeated on each sub-dataset, which enhanced the total
1064 data size to 3,254,352 × 3 particles, and yielded 1280 volumes in total that were used to compute
1065 the free-energy landscape of the substrate-engaged proteasome (Fig. 3b, c). Particle-voting on
1066 this energy landscape detected previously missing states (such as $E_{D0.2}$, $E_{D0.3}$, $E_{D1.1}$ and $E_{D1.2}$, etc.)
1067 and yielded previously determined states with improved map quality such as E_{A2} and E_{D2}.
1068 Guided by this initial discovery of new conformational states, extensive focused 3D
1069 classifications in AlphaCryo4D were performed, as described in detail in the next section, to
1070 discover novel ubiquitin-binding sites and hidden dynamics of proteasomal AAA-ATPase motor
1071 during single-nucleotide exchange. (3) The dataset of human NLRP3-NEK7 complex includes
1072 622,562 particles[23]. All particles were divided into 6 sub-datasets for particle shuffling, with the
1073 total data size enhanced to 622,562 × 3 images for volume bootstrapping. Given the small
1074 molecular size of the complex, the super-resolution pixel size of 0.42 Å and the box size of 240
1075 pixels were employed in image analysis. 480 volumes were bootstrapped to compute the free-
1076 energy landscape of the NLRP3-NEK7 complex (Extended Data Fig. 4k, l). The NLRP3-NEK7
1077 dataset exhibits certain degree of orientation preference. While AlphaCryo4D was able to
1078 retrieve 3 distinct NLRP3 conformations, the resulting map resolution is limited to ~4 Å.
1079 Although this may be already an improvement over the previous analysis of this dataset by the
1080 conventional approach, the result suggests that AlphaCryo4D does not necessarily overcome the
1081 potential issues of the orientation preference.

1082 **Focused 3D classification by AlphaCryo4D**

1083 To apply AlphaCryo4D to process the experimental dataset of the substrate-engaged human 26S
1084 proteasome[2], a focused 3D classification protocol using AlphaCryo4D was implemented to
1085 enhance its capability in discovering transient states of extremely low particle populations and in
1086 solving highly dynamic components that may be too small to be analyzed by conventional
1087 methods[7-9,18]. To study the local features of ubiquitin binding and substrate interactions, 3D
1088 masks corresponding to the local densities of interest were applied to all bootstrapped volume
1089 data, and the subset of interest on the free energy landscape was extracted to conduct a zoomed-
1090 in analysis. In this case, the free energy landscape calculated via masked volumes is expected to
1091 reflect the local structural variations of interest (Extended Data Fig. 6).

1092 To detect novel ubiquitin-binding sites in the proteasome, local masks were applied to focus
1093 on the features around the putative locations of ubiquitin chains. After particle shuffling for data
1094 augmentation, 732,666 × 3 particle images of the state E_A and E_B were utilized for computing the
1095 zoomed-in free energy landscape with 280 volumes. These particles were first aligned in a
1096 consensus alignment without any mask or resolution limit to restrict alignment parameter
1097 calculations. On the focused free energy landscape, only the region within the soft mask of the
1098 ubiquitin and its binding site was applied in the volume bootstrapping step, with the signals of
1099 the CP of the proteasome subtracted from each raw particle when dealing with the state E_A and
1100 E_B. Accordingly, the particle diameter applied in the CP subtracted proteasome was shrunk to
1101 274 Å, instead of 411 Å in the complete 26S proteasome. When the region around RPN2 masked
1102 for focused 3D classification to search for potential ubiquitin-like features, the total particle
1103 numbers were enhanced to 208,700 × 3 (E_{A1}), 240,475 × 3 (E_{A2}), 260,021 × 3 (E_B) and 129,492
1104 × 3 (E_{D2}). The free energy landscapes were computed with 80, 80, 80 and 40 masked volumes
1105 bootstrapped by upper resolution limitations of 15, 15, 15 and 20 Å, respectively. Several 3D
1106 classes with the particle numbers of 192,219, 2,539, 3,982 and 609 were obtained by the particle-
1107 voting procedure on the zoomed-in free energy landscape of state E_{A1}, while the case of state E_{A2}
1108 gave four classes containing 147,108, 5,842, 5,500 and 33,083 particles (Extended Data Fig. 6e,
1109 f). Likewise, the particle numbers of 3D classes on the zoomed-in free energy landscape of state
1110 E_B were 173,931, 5,117 and 9,754 (Extended Data Fig. 6g); and the zoomed-in free energy
1111 landscape of state E_{D2} resulted in four classes having 61,580, 6,192, 24,674 and 1,673 particles,
1112 respectively (Extended Data Fig. 6h).

1113 To detect and improve RPN1-bound ubiquitin densities, a local mask around RPN1 was used,
1114 with 15 Å resolution limit applied in the volume-bootstrapping step. The zoomed-in free energy
1115 landscape around state E_{A1} computed from 120 volumes resulted in five classes with the particle
1116 numbers of 128,161, 7,754, 6,557, 6,826 and 3,937. Five 3D classes on the zoomed-in free
1117 energy landscape of E_{A2}, also computed with 120 volumes, including 81,612, 27,483, 12,247,
1118 26,029 and 12,777 particles, were analyzed (Extended Data Fig. 6c, d). In the case of the
1119 ubiquitin-binding site on the α5 subunit of the CP, five 3D classes with the particle numbers of
1120 136,071, 19,351, 4,100, 131,570 and 4,932 were generated by particle voting on the zoomed-in
1121 free energy landscape of E_D computed with 120 volumes, which were bootstrapped from 326,409
1122 × 3 particles via the mask containing this ubiquitin-binding site and no high-resolution restriction
1123 (Extended Data Fig. 6i). During these analyses, all masked volume-bootstrapping steps were
1124 performed for 50 iterations, whereas unmasked 3D classifications were performed for 30
1125 iterations with the initial reference low-pass filtered to 60 Å. At the last step, 3D refinement and
1126 reconstruction of each class was done to finalize the high-resolution structure determination.
1127 To exploit intermediate conformations during the substrate translocation initiation, a zoomed-
1128 in free-energy landscape was computed for the focused 3D classification procedure. First, the
1129 free energy landscape of all 3,254,352 × 3 particles was computed and analyzed. Then the
1130 zoomed-in free energy landscape of the states E_C and E_D containing 2,521,686 × 3 particle
1131 images were computed from 1,000 volumes that were bootstrapped without masking or
1132 resolution restriction (Extended Data Fig. 6b). For further zoomed-in processes, the particles
1133 around the translocation initiation states (from E_C to E_{D0}) on this free energy landscape were
1134 extracted by the distance-based 3D classification strategy. Subsequently, these particles were
1135 augmented to the number of 410,098 × 3 to generate 160 volumes for the computation of the
1136 zoomed-in free energy landscape with the RP mask and no resolution restriction imposed in the
1137 volume bootstrapping, which led to the 3D classes E_{C1}, E_{C2}, and $E_{D0.1}$ with the particle number of
1138 68,506, 77,545, and 25,755, respectively (Extended Data Fig. 6j). Moreover, state $E_{D0.3}$ came
1139 from two clusters with 86,415 and 83,107 particles merged together on the unmasked free energy
1140 landscape, and the classes $E_{D0.2}$ and $E_{D1.1}$ including 105,081 and 51,808 particles, respectively,
1141 were also obtained after particle voting on this free energy landscape. In the local areas of the
1142 state E_{D1} on the energy landscape, two clusters with 80,841 and 94,273 particles were merged to
1143 reconstruct the high-resolution structure of state $E_{D1.2}$, while states $E_{D1.1}$ and $E_{D1.3}$ with 40,696

1144 and 145,506 particles, respectively, were separated out from the clusters on this unmasked free
1145 energy landscape. In these studies, the maximum number of iterations in the 3D classifications of
1146 volume bootstrapping was 30, with the initial reference low-pass filtered to 60 Å routinely.
1147 Beyond resolving significantly more conformers from the same dataset, AlphaCryo4D also
1148 allows us to push the envelope of the achievable resolution of dynamic components and key
1149 metastable states due to its advantage in keeping more particles without sacrificing
1150 conformational homogeneity. To improve the resolution of state E_{D2}, a rigorous particle voting
1151 procedure was performed in each cluster on the unmasked free energy landscape (Fig. 3b, c),
1152 which improved the overall quality of particle dataset while classifying significantly more
1153 particles to this E_{D2} conformational class. Next, we conducted a focused 3D classification by
1154 using AlphaCryo4D to calculate the zoomed-in free energy landscape of the entire E_{D2} dataset to
1155 detect any potential conformational changes within this class. Five clusters near the energy wells
1156 of state E_{D2}, whose particle numbers were 154,661, 243,799, 198,221, 179,257 and 106,047,
1157 were investigated by separate high-resolution 3D refinement and reconstruction. The resulting
1158 refined density maps at 3.0-3.5 Å were found to be all in an identical conformation as previously
1159 reported[2]. These five clusters were then merged together to refine a final 3D density map of state
1160 E_{D2}. Thus, AlphaCryo4D allowed us to obtain a new E_{D2} dataset that appears to retain high
1161 conformational homogeneity while including three-fold more particles, which improves its 3D
1162 reconstruction from the previously published resolution at 3.2 Å to 2.5 Å, measured by gold-
1163 standard Fourier shell correlation (FSC) at 0.143-cutoff. By contrast, in our previous work[2], we
1164 had attempted to include more E_{D2}-compatible 3D classes from 3D maximum-likelihood
1165 classification in RELION, which resulted in lower resolution at 3.3 Å by doubling the E_{D2}
1166 dataset, indicating that including more particles by conventional methods gave rise to higher
1167 heterogeneity in the class presumably due to increased misclassification.

1168 **Analysis of doubly and singly capped proteasomes**

1169 Previous cryo-EM analyses of the proteasomal states were nearly all focused on the RP-CP
1170 subcomplex, by converting double-cap (DC) proteasome particles to pseudo single-cap (SC)
1171 proteasome, which was always mixed with true SC particle images, in order to improve the
1172 resolution with conventional methods[2,14-16,47,48]. As a result, the cryo-EM density of the CP gate
1173 in the other side distal to the RP in the RP-CP subcomplex has been an average of closed and
1174 open states with unknown stoichiometry. This has made it impossible to appreciate the difference

between the SC and DC proteasomes in the previous studies. To remove this ambiguity, we reconstructed 8 density maps of the true SC proteasome and 36 density maps of the true DC proteasome including all possible combination of the 8 major RP-CP states. To reconstruct the density maps of the DC proteasome, pseudo-SC particles corresponding to 8 different RP states were voted out from the free energy landscape, with the sub-states belonging to the same RP state combined together. Then the particles with one RP-CP were extracted from the particle stacks to refine the RP and CP density maps with RP and CP contour masks applied in the local search step in RELION, respectively. For each reconstruction of the DC proteasome, two RP density maps on the opposite sides of the CP were expanded from 600 × 600 × 600 pixels to 800 × 800 × 800 pixels using RELION and aligned by the density of CP in Chimera before being merged together.

Counting the particle number of the 36 states of the DC proteasome, we could derive the distribution of the DC states, p_{ij}, and that of RP p_i only, where i and j denote the states of two RPs in the same DC proteasome. Based on the value of p_{ij} and total particle number, the experimental state distribution of the DC proteasome was plotted for quantitative analysis in two dimensions with respect to the states of two RPs in the same DC proteasome (Fig. 3e). If the states of two RPs of the same DC proteasome were independent of each other, the predicted state distribution $\tilde{p}_{ij}$ of the DC proteasome can be calculated as:

$$\tilde{p}_{ij} = p_i \cdot p_j$$

By using the total particle number and experimentally measured p_i, the 2D state distribution of the DC proteasome with two uncoupled RPs was calculated for further comparison to investigate the conformational entanglement effect of the two RP states (Fig. 3f-h).

Atomic model building and refinement

To build the initial atomic model of the newly discovered states, we use previously published proteasome structures as a starting model and then manually improved in Coot[49]. For the conformational states at resolutions lower than 5 Å, pseudo-atomic modelling was conducted in the following steps. First, each subunit was fitted as a rigid body, often in UCSF Chimera[50] as well as in Coot[49]. Then, the local structural domains and secondary structure elements were fitted as a rigid body, with linking loops flexibly fitted and modelled. After the mainchain structures were well fitted, no further fitting of the sidechain rotamers were pursued due to insufficient resolution except for energy minimization to remove unrealistic side-chain clashes. For the

1206 conformational states at resolutions higher than 5 Å, the mainchain traces were first fit in Coot.
1207 Then, extensive fitting, adjustment and optimization of sidechain rotamers were conducted
1208 through local real-space refinement and manual rectification in Coot to the degree commensurate
1209 to the map resolution and quality. Atomic model refinement was conducted in Phenix[51] with its
1210 real-space refinement program. We used both simulated annealing and global minimization with
1211 NCS, rotamer and Ramachandran constraints. Partial rebuilding, model correction and density-
1212 fitting improvement in Coot[49] were iterated after each round of atomic model refinement in
1213 Phenix[51]. The improved atomic models were then refined again in Phenix, followed by
1214 rebuilding in Coot[49]. The refinement and rebuilding cycle were often repeated for three rounds or
1215 until the model quality reached expectation (Extended Data Table 2). All figures of structures
1216 were plotted in Chimera[50], PyMOL[52], or ChimeraX[53]. Local resolutions of cryo-EM density
1217 maps were evaluated using ResMap[54] or Bsoft Blocres program[55]. Structural alignment and
1218 comparison were performed in both PyMOL and Chimera. Electrostatic surfaces were calculated
1219 by APBS plugin[56] in PyMOL.
1220 Given a large range of variations of local resolution in an expanded number of proteasome
1221 states and substates, as well as reconstructions with different stoichiometric ratio of RP versus
1222 CP, additional caveats and cautions were practiced in order to avoid misinterpretation and
1223 overall-fitting of atomic and pseudo-atomic models. First, when fitting the ubiquitin structure to
1224 the low-resolution local density, we consider both the existing homologous structural models as a
1225 modelling reference. Specifically, the fitting of diubiquitin to the density on RPN2 in states $E_{A2.1}$,
1226 $E_{A2.2}$, and $E_{B.2}$, we took the NMR structure of the yeast di-ubiquitin-bound Rpn1 T1 site as a
1227 reference, because of the high structural homology between RPN1 and RPN2. For the fitting of
1228 RPN10-bound density, we also took into account the electrostatic complementarity (Extended
1229 Data Fig. 10). Second, even within an overall high-resolution cryo-EM map, it often presents
1230 certain local densities at a lower local resolution due to poor occupancy of ligands or flexibility
1231 of less well-folded segments. For example, for the nucleotide in RPT5 in states $E_{D0.1}$ to $E_{D1.3}$, the
1232 high-resolution atomic model of ADP refined from other states like E_{C1} were used to fit these
1233 lower-local-resolution densities as a rigid body. However, the B-factors of the fitting atoms of
1234 ADP in RPT5 were reported to be more than twice higher than those of other nucleotides,
1235 indicating its partial occupancy or unstable binding. Thus, ADP fitting in RPT5 should be
1236 regarded tentative for the most or for the purpose of evaluation of nucleotide states rather than a

1237 reliable high-resolution atomic modeling. Similarly, the atomic models of these locally low-
1238 resolution features were only further adjusted with strict stereochemical constraints when the
1239 map resolution and features permit. Third, for the CP gate at the other side opposite to the RP in
1240 the RP-CP subcomplex reconstructed from a mixture of true and pseudo-SC proteasomes
1241 (converted from the DC proteasomes), their local densities in states $E_{D0.1}$ to E_{D2} appears to be an
1242 average of the open and closed states, and thus are weaker in amplitude than the rest of the CP.
1243 In the atomic model building of these reconstructions, we chose to model them with the closed
1244 CP gate state as long as their density resolution allows atomic modeling. This issue was
1245 completely solved when we separated the 3D classes of the SC and DC proteasomes and
1246 reconstructed their states respectively, where the atomic modelling of any CP gate no longer
1247 suffers from such ambiguities.

1248 **Quantum mechanical calculation**

1249 First-principles calculations on the electronic structures of the substrate-proteolytic site complex
1250 were conducted as described. In brevity, local coordinates of the substrate-bound CP near the
1251 catalytic site at residue Thr1 were taken out from the experimentally fitted atomic models of CP
1252 and the substrate, in both E_A and E_{D2} conformations. The proteolytic site is the Thr1 residue at
1253 the β2 subunit but extended along the chain for another two residues to make the system less
1254 finite. Hydrogen atoms are added to complete the residues, and to saturate the system
1255 boundaries. The structural relaxations and electronic structure calculation were carried out using
1256 the density functional theory (DFT) method with norm-conserving pseudopotentials as
1257 implemented in the SIESTA code[57]. To set up the initial conditions of the finite system, the
1258 hydrogen atom in the hydroxy group of Thr1 is manually relocated to the nearby nitrogen atom
1259 in the same residue, corresponding to the initial proton transfer in the catalytic mechanism. All
1260 hydrogen atoms were subsequently optimized without symmetric restrictions using the conjugate
1261 gradient algorithm and a 0.04 eV/Å maximum force convergence criterion while keeping the rest
1262 of the system fixed. The generalized gradient approximation (GGA) exchange-correlation
1263 density functional PBE[31] was employed together with a double-zeta plus polarization basis set,
1264 and a mesh cutoff of 200 Ry (corresponds to 0.23 Å smallest grid size). The charge density and
1265 charge density difference contour maps were plotted with the Siesta Utility programs denchar
1266 and Python, respectively.

1267 **Data availability**

The three-dimensional cryo-EM density maps of all new states are deposited into the Electron Microscopy Data Bank (EMDB) (www.emdatasource.org) under accession numbers to be provided upon formal publication of this manuscript). The coordinates are deposited in the Protein Data Bank (PDB) (www.wwpdb.org) (with accession numbers to be provided upon formal publication of this manuscript). Raw data are deposited into the Electron Microscopy Pilot Image Archive (www.ebi.ac.uk/pdbe/emdb/empiar) (with accession numbers to be provided upon formal publication of this manuscript). Source code of AlphaCryo4D is freely available for download (http://ipccsb.dfci.harvard.edu/alphacryo4d/).

Acknowledgments. The authors thank Q. Ouyang, A. Goldberg, D. Finley, S. Elsasser, M. Kirschner, Y. Lu, and for constructive discussions. This work was funded in part by the Natural Science Foundation of Beijing Municipality (grant No. Z18J008/Z180016), the National Natural Science Foundation of China (grant No. 11774012) and a gift academic grant from Intel Corporation. The cryo-EM data were collected at the Cryo-EM Core Facility Platform and Laboratory of Electron Microscopy at Peking University. The data processing was performed in the High-Performance Computing Platform at Peking University.

Author contributions. Y.M. and Z.W. conceived this study, devised the methodology and wrote the paper. Z.W. developed the deep learning system and conducted numerical studies of the system using the synthetic datasets. Z.W. and S.Z analyzed the experimental cryo-EM datasets and refined the density maps. W.L.W. conducted the quantum mechanical simulation. Y.M. supervised this study, verified the density maps, built and refined the atomic models, interpreted the data and drafted the manuscript with inputs from all authors.

Competing interests. The authors declare no competing financial interests.

Correspondence and requests for materials should be addressed to Y.M.

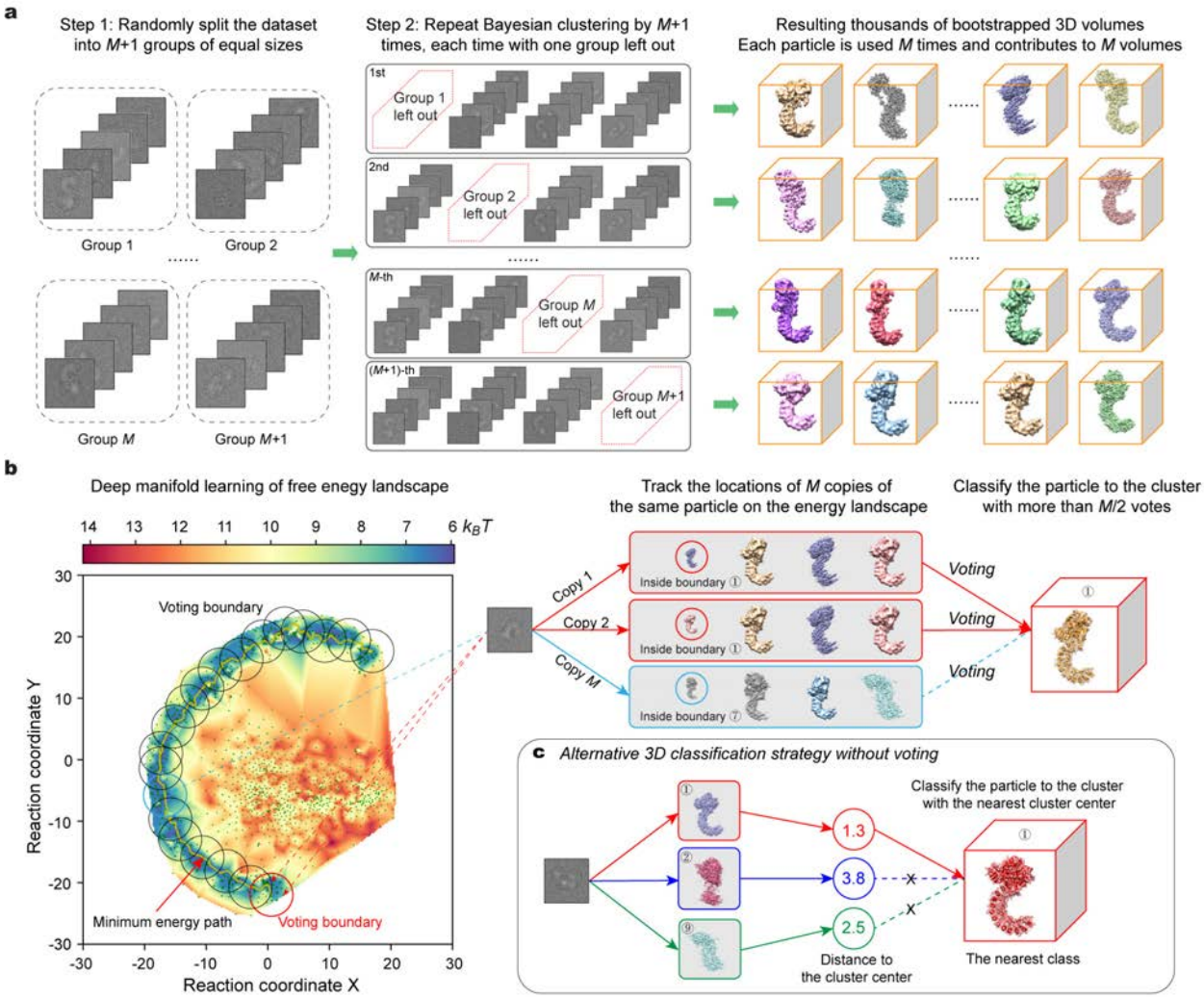

Extended Data Fig. 1. Detailed algorithmic design of particle shuffling and voting in AlphaCryo4D. a, Schematic showing the method of particle shuffling for data augmentation and bootstrapping of 3D volumes. In the step 1, all particles are split randomly into $M + 1$ groups equally. Then the step 2 carries out the Bayesian clustering for reconstructions of 3D density maps within each of the $M + 1$ particle sets that are shuffled via the leave-one-group-out approach. After these two steps, thousands of 3D volumes are generated for the subsequent 3D deep learning, with each particle contributing to M volumes. **b**, Schematic showing the algorithmic concept of energy-based particle voting for 3D classification. The left panel shows the free energy landscape obtained by deep manifold learning. After clustering along the minimum energy path, all M locations of each particle on the free energy landscape can be tracked to cast M votes. A vote of the particle is only counted for the cluster when it is mapped within the voting boundary of the cluster, as indicated by the circles marked on the free-energy

landscape. Eventually, this particle is classified to the 3D cluster with over $M/2$ votes from this particle. **c**, Alternative distance-based 3D classification method as a control in the analysis of algorithmic performance of particle voting. Instead of particle voting, each particle is directly classified to the cluster with the nearest clustering center among the M volume data points in the distance-based 3D classification strategy.

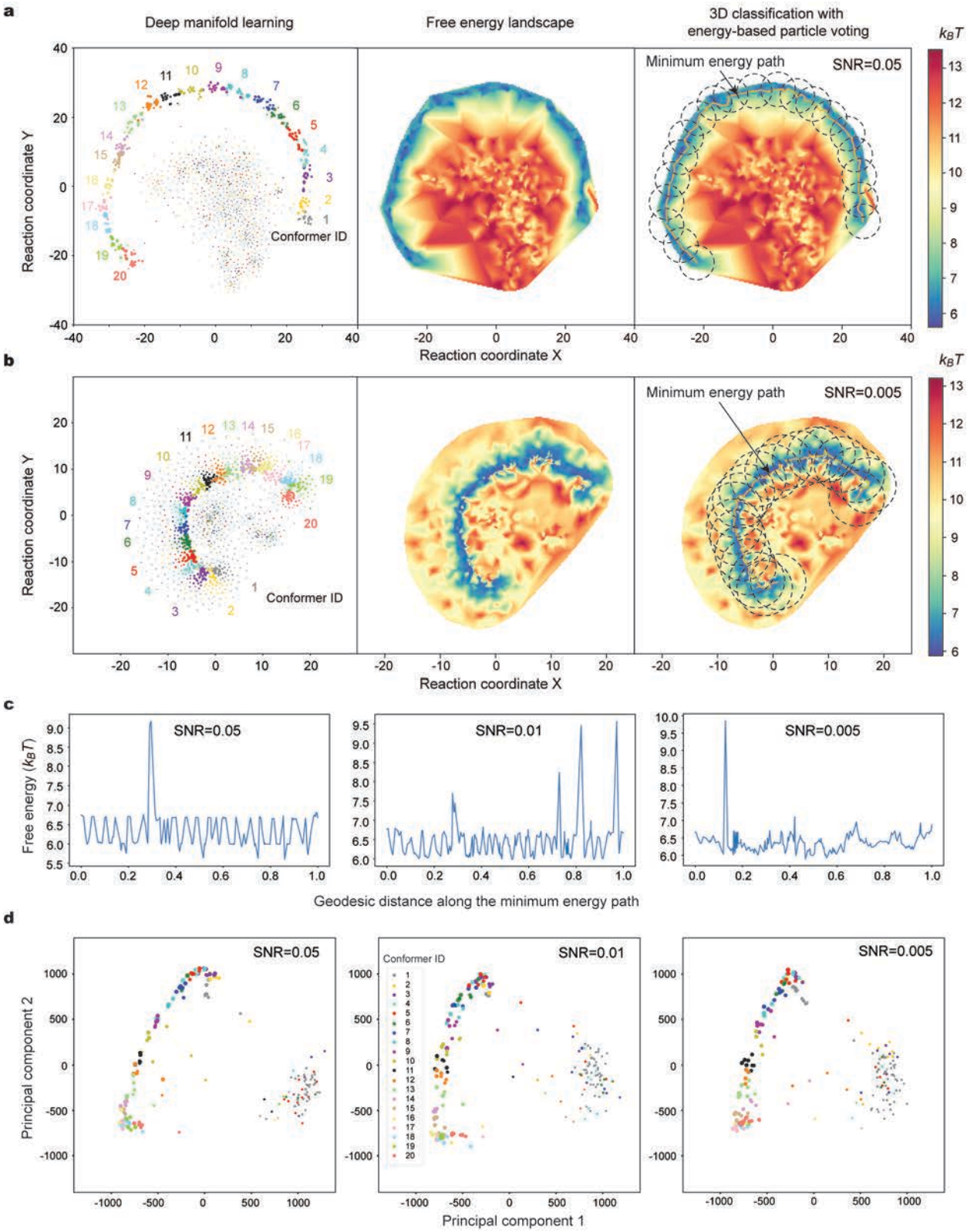

Extended Data Fig. 2. Blind assessments of AlphaCryo4D and its comparison with the 3D PCA method using the simulated heterogeneous NLRP3 datasets of different SNRs. a and

b, Reconstruction of the free energy landscape of the simulated NLRP3 datasets at SNRs of 0.05 (**a**) and 0.005 (**b**) by the t-SNE algorithm using the bootstrapped volumes and their corresponding feature maps. Colors in the left panels indicate the ground truth of 3D volume data points. **c**, Free energy profiles along the MEP calculated by the string method in the 2D energy landscapes of the simulated NLRP3 datasets at SNRs of 0.05 (left), 0.01 (middle) and 0.005 (right). **d**, Dimensionality reduction and 3D classification of the simulated datasets at three distinct SNRs by the 3D PCA method as the control of our algorithm evaluation. Colors of data points indicate the ground truth of their corresponding 3D volumes.

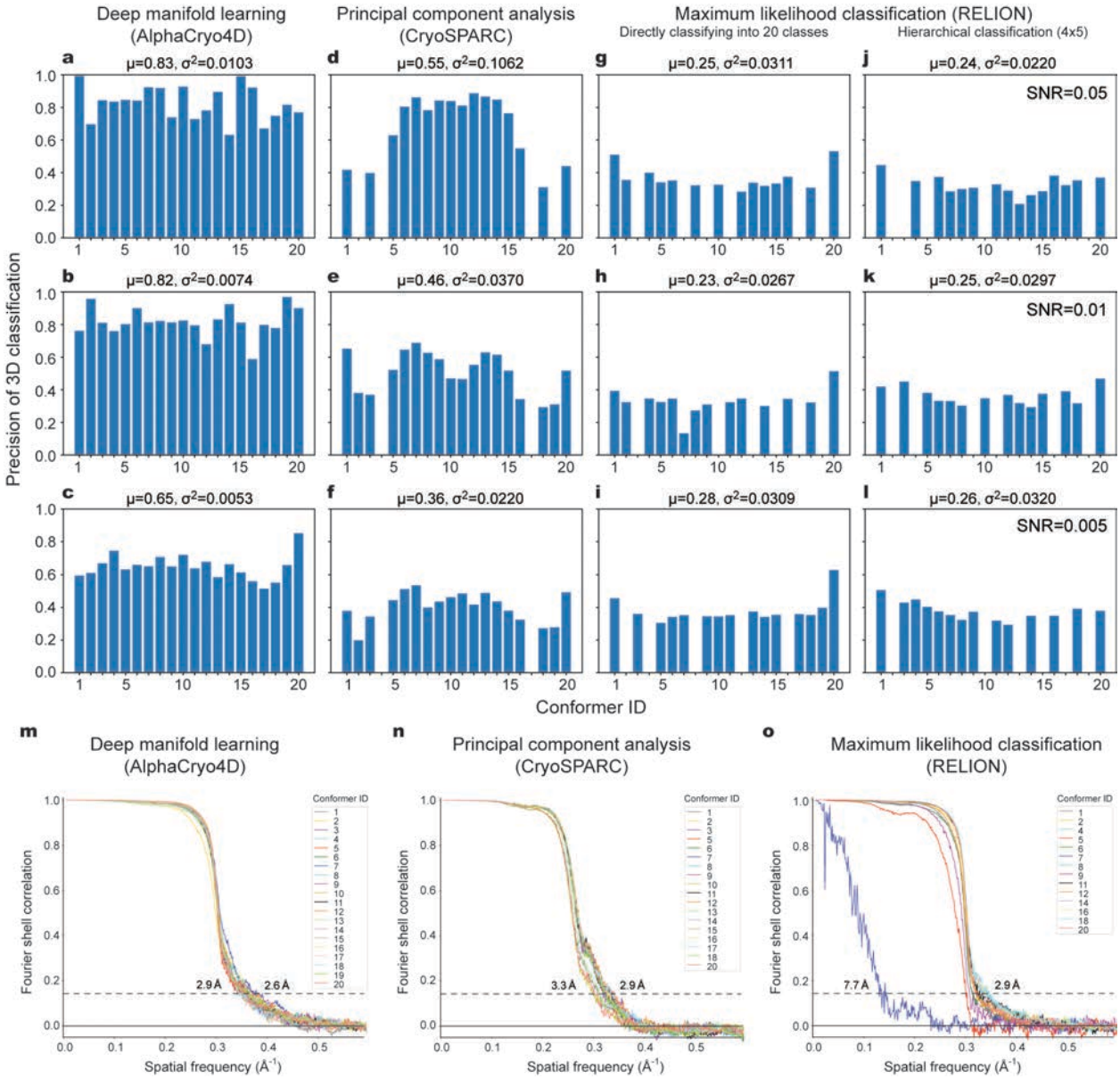

Extended Data Fig. 3. Performance comparison of AlphaCryo4D with existing methods using the simulated heterogeneous NLRP3 datasets of different SNRs. a-l, 3D classification precision of the simulated datasets by AlphaCryo4D (**a-c**), PCA in CryoSPARC (**d-f**) and maximum-likelihood classification in RELION (**g-l**). The results of SNRs of 0.05 (**a, d, g, j**), 0.01 (**b, e, h, k**) and 0.005 (**c, f, i, l**) are shown on three rows for side-by-side comparison. On the top of each panel, the symbols of μ and σ^2 denote the mean and variance of precision, respectively, with the values of missing classes treated as zeros. In the maximum-likelihood classification of RELION, both direct and hierarchical strategies are compared in the study. **m-o**, The gold-standard FSC of the 20 maps resulting from 3D classification by AlphaCryo4D (**m**), of

the 18 maps resulting from the 3D classification by PCA in CryoSPARC (**n**), and of the 14 maps resulting from the maximum-likelihood 3D classification in RELION (**o**) on the simulated data of 0.01 SNR. They correspond to the precision results presented in panels (**b**), (**e**) and (**h**), respectively.

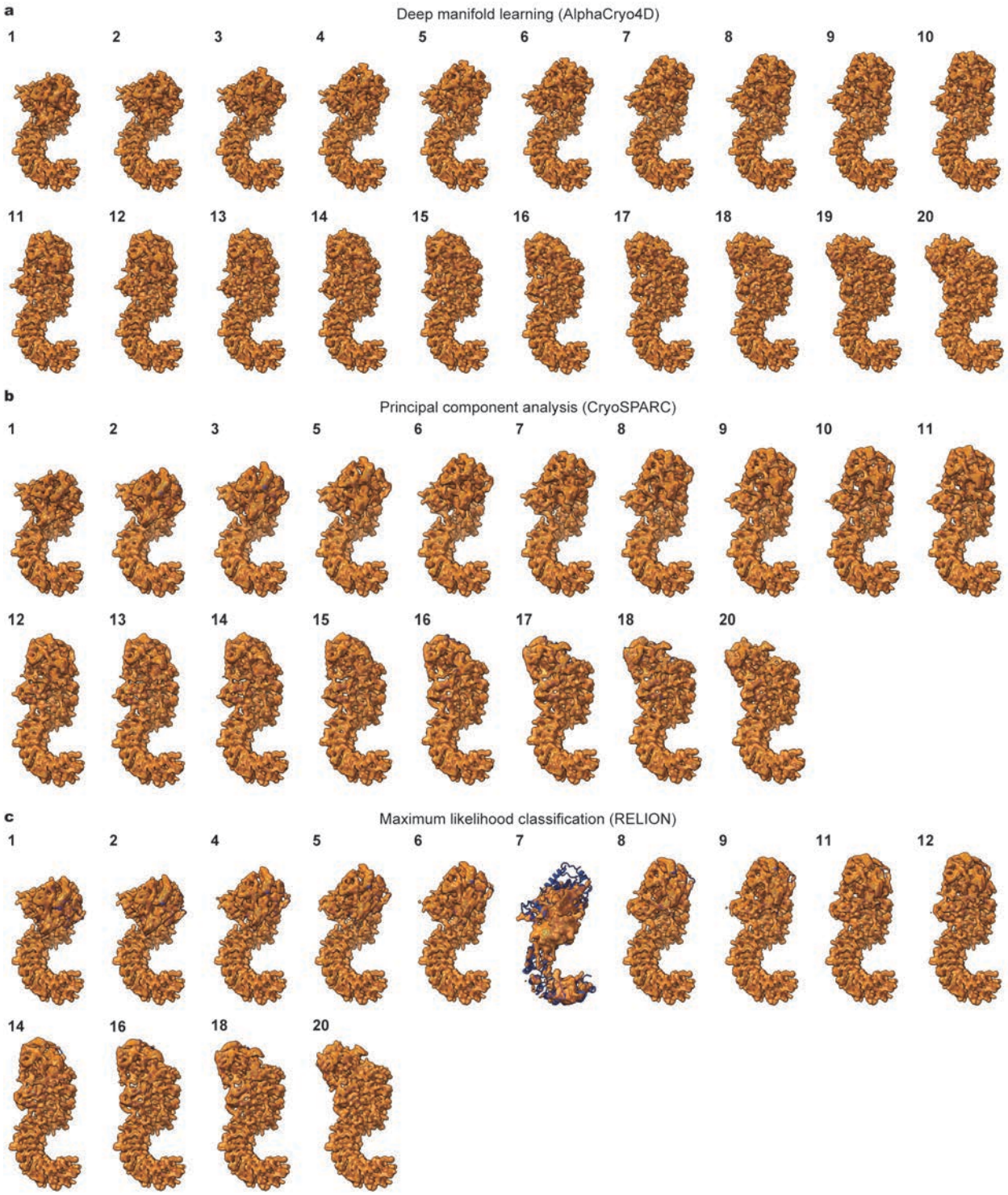

Extended Data Fig. 4. Map assessment of AlphaCryo4D in reconstructions of conformational continuum in comparison with conventional methods on the simulated data of 0.01 SNR. a, The 20 maps of NLRP3 resulting from the 3D classification by AlphaCryo4D. **b**, The 18 maps of NLRP3 resulting from the 3D classification by PCA in CryoSPARC. **c**, The

14 maps of NLRP3 resulting from the 3D classification by ML3D in RELION. All maps are shown in transparent surface representations superimposed with their corresponding atomic models of the ground truth in cartoon representations, which are fitted to the maps as rigid bodies without further atomic modelling. The conformer ID numbers are marked on the upper left of each map panel. The results shown in panels (**a**), (**b**) and (**c**) correspond to the FSC results shown in panels (**m**), (**n**) and (**o**) of Extended Data Fig. 3, respectively.

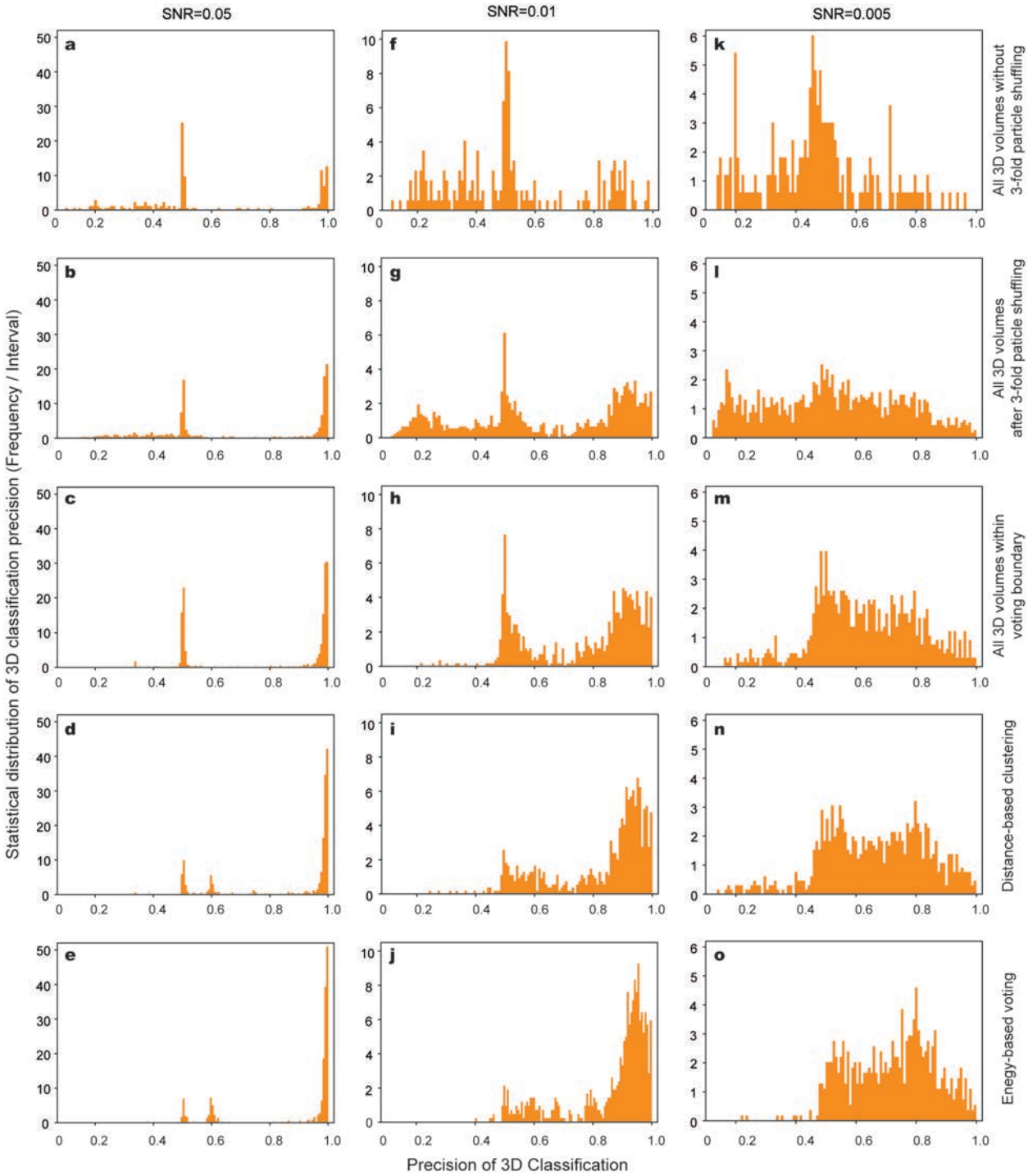

Extended Data Fig. 5. Mechanistic characterizations of the improvement of 3D classification precision in the intermediate steps of AlphaCryo4D using the simulated NLRP3 datasets of three typical SNRs. a-e, Precision analysis on the simulated data of SNR of 0.05. **f-j**, Precision analysis on the simulated data of SNR of 0.01. **k-o**, Precision analysis on the simulated data of SNR of 0.005. **a**, **f**, **k**, Statistical distribution of 3D classification precision in

bootstrapped 3D volumes without particle shuffling. **b**, **g**, **l**, Distribution of 3D classification precision in bootstrapped 3D volumes after 3-fold particle shuffling. **c**, **h**, **m**, Distribution of classification precision in bootstrapped 3D volumes screened by voting boundary on the free energy landscape. **d**, **i**, **n**, Distribution of classification precision in bootstrapped 3D volumes after distance-based 3D clustering in the absence of particle voting as a control. **e**, **j**, **o**, Distribution of classification precision in bootstrapped 3D volumes after energy-based particle voting.

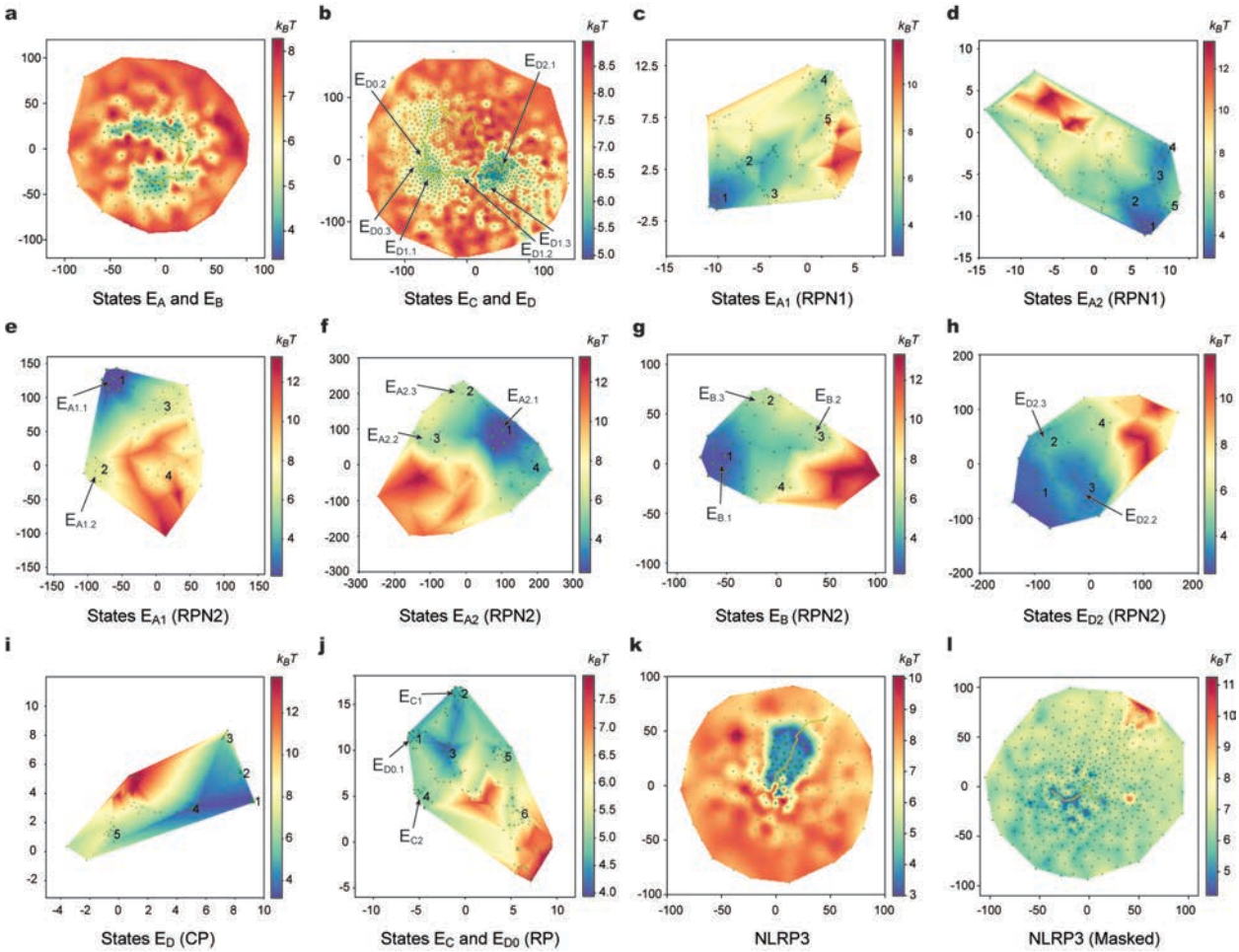

Extended Data Fig. 6. The zoomed-in free-energy landscape used for focused 3D classifications of AlphaCryo4D on the experimental cryo-EM datasets for finding new states of the substrate-bound proteasome. a-j, The zoomed-in local energy landscapes of the substrate-bound human proteasome by AlphaCryo4D are shown for state E_A and E_B in (**a**), for states E_C and E_D in (**b**), for states E_{A1} and E_{A2} with 3D mask focusing on RPN1 in (**c**) and (**d**), for states E_{A1}, E_{A2}, E_B and E_{D2} with 3D masking around RPN2 in (**e**), (**f**), (**g**) and (**h**), respectively, for combined states of E_D with masking around CP (**i**), and for combined states of E_C ad E_{D0} with 3D mask focusing on the RP (**j**). **k** and **l**, The energy landscape computed from the experimental cryo-EM dataset of the NLRP3-NEK7 complex without (**k**) and with a global contour mask (**l**).

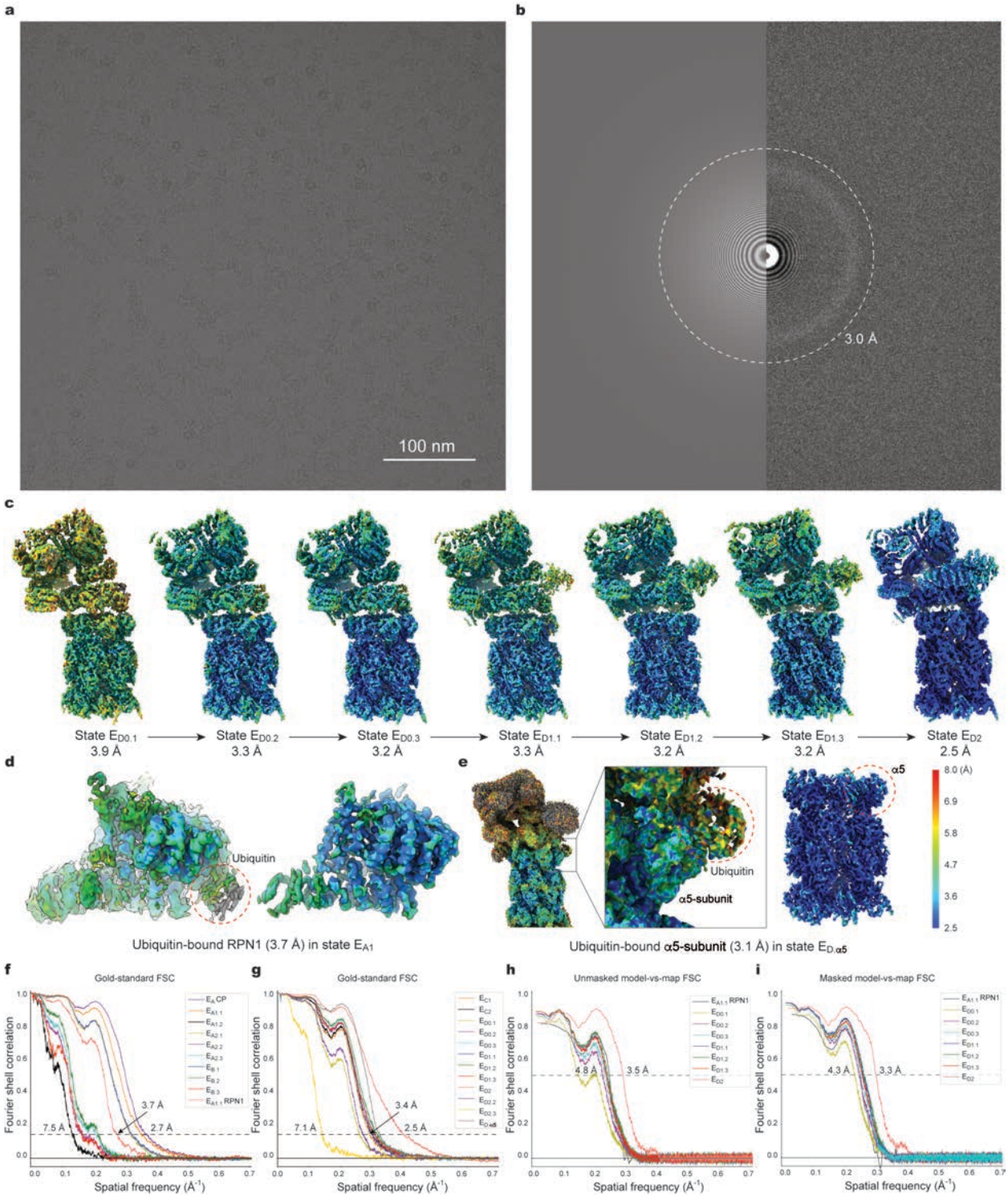

Extended Data Fig. 7. Cryo-EM reconstructions and resolution assessment of novel proteasomal states determined by AlphaCryo4D. a, A typical raw micrograph of the substrate-bound human proteasome recorded under the super-resolution counting mode of Gatan K2 Summit direct electron detector. **b**, The power spectrum of the micrograph shown in panel

1397 (**a**), with the 3 Å resolution ring marked by the dashed circle. **c**, Local resolution measurement of
1398 the seven sequential states corresponding to the open CP gate states $E_{D0.1}$ to E_{D2}. **d**, The local
1399 resolution measurement of the density maps of ubiquitin-bound RPN2 structure in state E_{A1} at
1400 two different contour levels. **e**, The local resolution measurement of the CP in state $E_{D.\alpha5}$, with a
1401 ubiquitin-moiety bound to the α5 subunit. The right panel shows the CP density map at higher
1402 contour level. The color bar for local resolutions is shown for all panels in **c**-**e**, which were all
1403 measured by ResMap[54]. **f** and **g**, The gold-standard FSC plots of the 20 conformers of the RP-CP
1404 subcomplex. **h** and **i**, The FSC curves calculated between the experimental cryo-EM maps and
1405 their corresponding atomic models for newly discovered states or improved states without (**h**)
1406 and with (**i**) masking in the calculations.

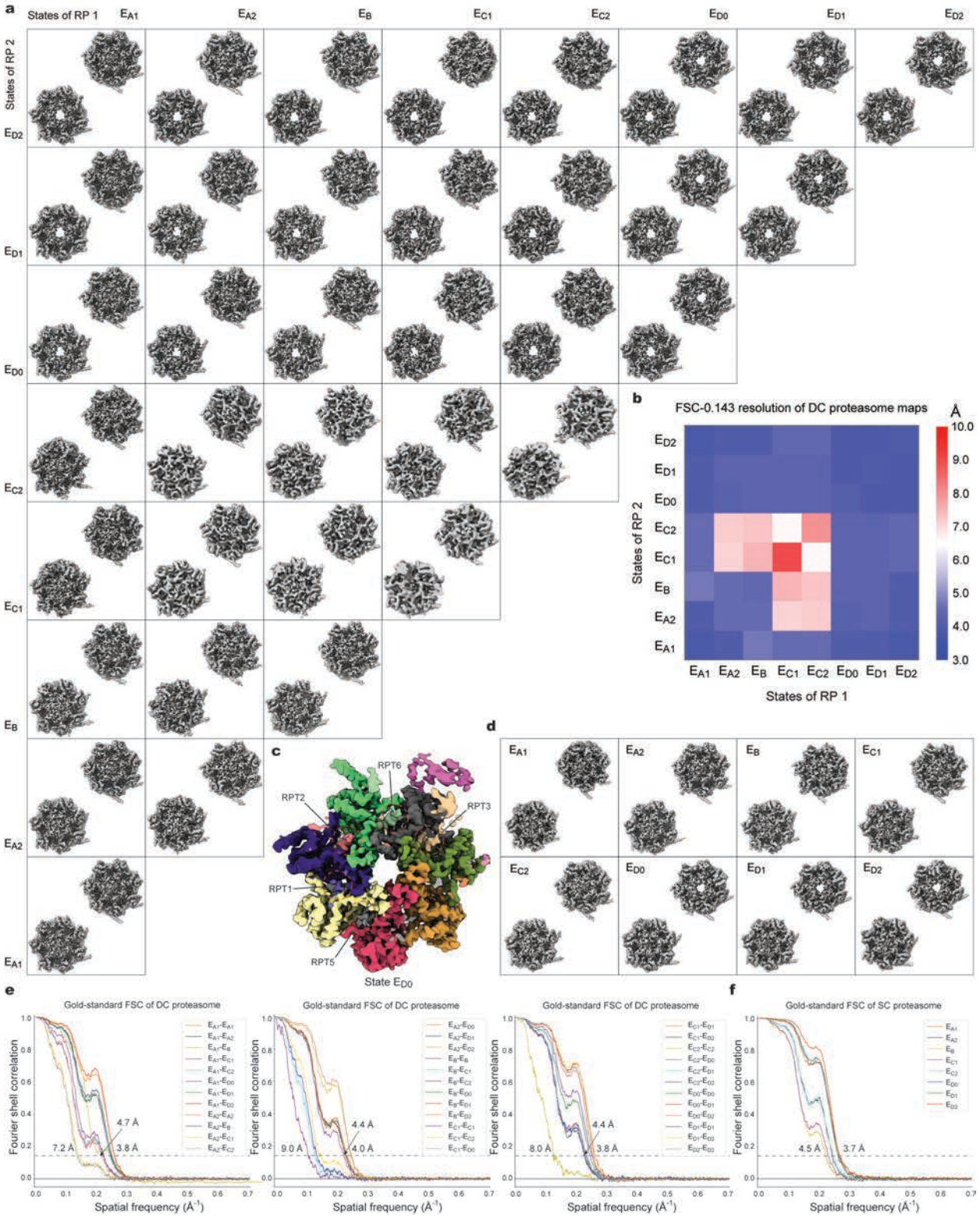

Extended Data Fig. 8. Cryo-EM analysis of the doubly capped (DC) and singly capped (SC) proteasomes. a, The CP gate states of the 36 density maps of distinct conformational states of the DC proteasome. All density maps shown are low-pass filtered to their measured resolutions

1411 by the gold-standard FSC-0.143 cutoff without amplitude correction of B-factors. **b**, The FSC-
1412 0.143 resolution matrix of the 36 DC proteasomal states. **c**, The RP-CP interface of state E_{D0},
1413 showing five C-terminal tails inserted into the inter-subunit surface pockets of α-ring. **d**, The CP
1414 gate states of the 8 density maps of distinct conformational states of the SC proteasome, with the
1415 upper right image in each panel corresponding to the RP-proximal side of the CP gate, and the
1416 lower left image to the RP-distal side of the CP gate. **e**, The gold-standard FSC plots of the 36
1417 conformers of the DC proteasome. **f**, The gold-standard FSC plots of the 8 conformers of the SC
1418 proteasome.

a
E_{A1}
E_{A2}
E_B
E_{C1}
E_{C2}
E_{D0}
E_{D1}
E_{D2}
b
E_{A1}-E_{A1}
E_{A1}-E_{A2}
E_{A1}-E_B
E_{A1}-E_{C1}
E_{A1}-E_{C2}
E_{A1}-E_{D0}
E_{A1}-E_{D1}
E_{A1}-E_{D2}
E_{A2}-E_{A2}
E_{A2}-E_B
E_{A2}-E_{C1}
E_{A2}-E_{C2}
E_{A2}-E_{D0}
E_{A2}-E_{D1}
E_{A2}-E_{D2}
E_B-E_B
E_B-E_{C1}
E_B-E_{C2}
E_B-E_{D0}
E_B-E_{D1}
E_B-E_{D2}
E_{C1}-E_{C1}
E_{C1}-E_{C2}
E_{C1}-E_{D0}
E_{C1}-E_{D1}
E_{C1}-E_{D2}
E_{C2}-E_{C2}
E_{C2}-E_{D0}
E_{C2}-E_{D1}
E_{C2}-E_{D2}
E_{D0}-E_{D0}
E_{D0}-E_{D1}
E_{D0}-E_{D2}
E_{D1}-E_{D1}
E_{D1}-E_{D2}
E_{D2}-E_{D2}

1419

1420 **Extended Data Fig. 9. 44 cryo-EM reconstructions of the SC and DC proteasomes classified**
1421 **from the same experimental dataset by AlphaCryo4D. a**, The density maps of 8 distinct
1422 conformational states of the SC proteasome. **b**, The density maps of 36 distinct conformational
1423 states of the DC proteasome. All maps are filtered to their respective gold-standard FSC-0.143
1424 resolutions without amplitude correction of B-factors and are differentially colored by their
1425 subunits in ChimeraX[53].

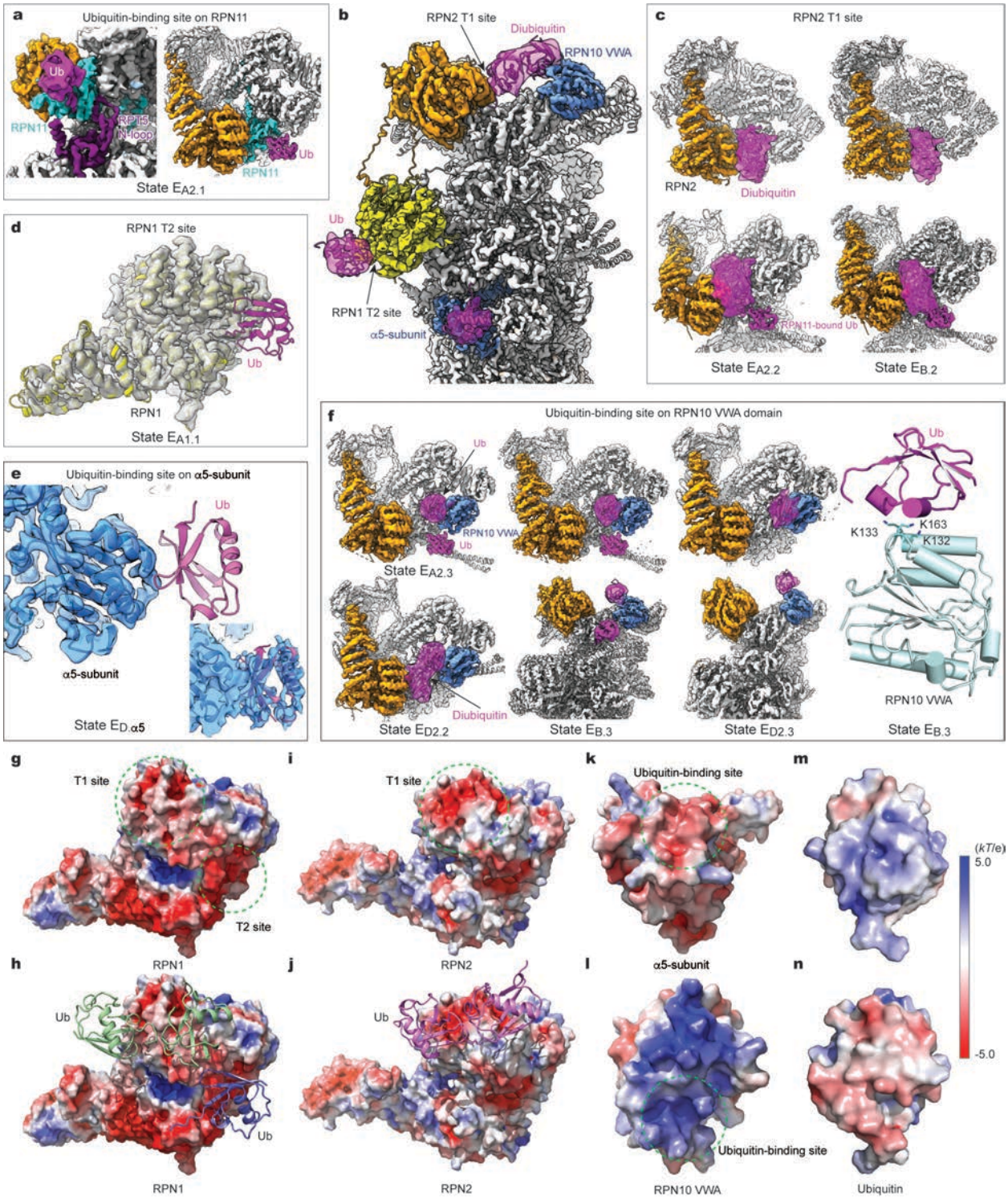

Extended Data Fig. 10. Structural analysis of ubiquitin-binding sites at high resolution. a, Cryo-EM density of state $E_{A2.1}$ shows the improved resolution localized around RPN11-bound ubiquitin and the RPT5 N-loop as compared to previously determined state E_{A2}. Ub, ubiquitin. **b**, High-resolution cryo-EM density of state E_{D2} superimposed with ubiquitin densities in state $E_{D2.2}$

highlighted as magenta, showing that a diubiquitin chain in contact with both the RPN2 T1 site and the RPN10 VWA domain. The atomic model of state $E_{D2.2}$ in cartoon representation is superimposed with the density map. **c**, Closeup view of the RPN2-bound diubiquitin density in states $E_{A2.2}$ (left column) and $E_{B.2}$ (right column) in two different perspectives, with the lower row showing the coexistence of the RPN11-bound ubiquitin and the RPN2-bound diubiquitin. **d**, The refined 3.7-Å RPN1 density map from state $E_{A1.1}$ in transparent surface representation superimposed with its atomic model with ubiquitin bound to the RPN1 T2 site. **e**, Closeup view of the α5-subunit bound with ubiquitin in the refined 3.1-Å density map of state $E_{D.\alpha5}$. The cryo-EM density of the α5-subunit is shown in transparent surface representation superimposed with its atomic model. Inset shows the ubiquitin density in transparent surface representation superimposed with its atomic model. **f**, Closeup views of the RPN10-bound ubiquitin densities in states $E_{A2.3}$, $E_{B.3}$, and $E_{D2.3}$. Right panel shows the pseudo-atomic model of ubiquitin interaction with the RPN10 VWA domain. **g-l**, The electrostatic surfaces of RPN1, RPN2, RPN10 and α5-subunit show the charge complementarity of the RPN1 T1 and T2 (panels **g**, **h**), RPN2 T1 (panels **i**, **j**) and α5-binding (panel **k**) sites of ubiquitin are all acidic. By contrast, the RPN10 VWA site is basic (panel **l**), suggesting that it may bind the acidic side of the ubiquitin molecule. **m** and **n**, The electrostatic surface of the ubiquitin shows one side that is basic (panel **m**) and the other side acidic (panel **n**).

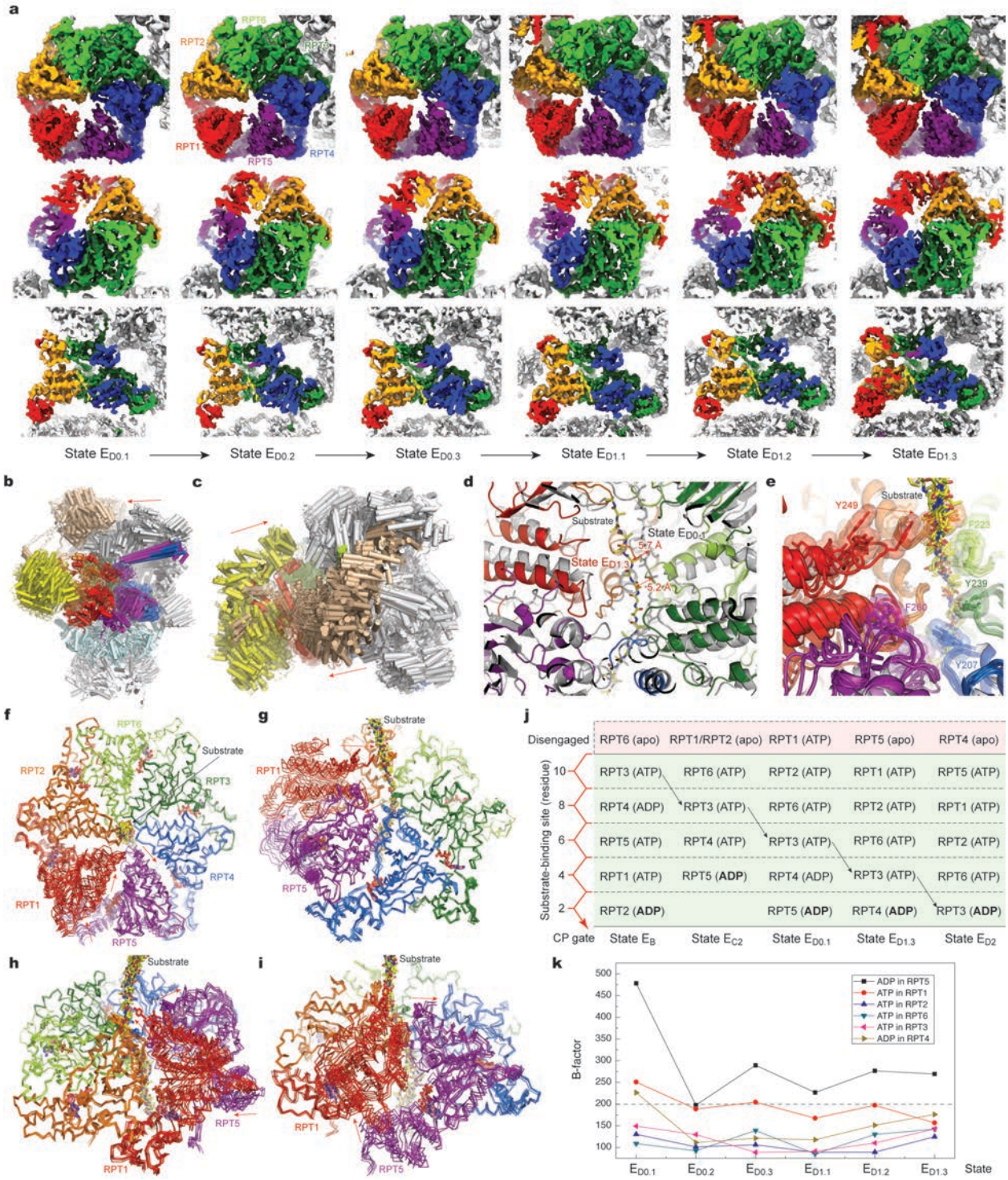

Extended Data Fig. 11. Cryo-EM structures of six sequential intermediate states between E_{C2} and $E_{D1.3}$. a, Cryo-EM density maps of the AAA-ATPase motor in six sequential states from $E_{D0.1}$ to $E_{D1.3}$ from three different viewing angles. The substrate densities are highlighted in yellow. **b**, Superposition of the seven structures in cartoon representations from a lateral

1454 perspective, with all structures aligned together based on their CP structures, showing the RP
1455 movements relative to the CP. **c**, Superposition of the six structures in cartoon representations
1456 from a top-view perspective, with all structures aligned together based on their CP structures. **d**,
1457 Measurement of substrate movement between states $E_{D0.1}$ and $E_{D1.3}$ relative to the CP, suggesting
1458 that the substrate is translated ~5-6 Å during the process of ADP release in RPT5 and of RPT1
1459 re-association with the substrate. **e**, The closeup view of the pore-1 loop interaction with the
1460 substrate with all six states superimposed after aligned together based on the structures of RPT3,
1461 RPT4 and RPT6. **f-i**, Superposition of the six sequential states with their RPT3, RPT4 and RPT6
1462 aligned together. Red arrows show the direction of subunit movements in RPT1 and RPT5. **j**, A
1463 diagram illustrating the axial stepping of the substrate-interacting pore-1 loops that is coupled
1464 with ATP hydrolysis in the RPT subunits, revised from the previously published results based on
1465 the present study[2]. **k**, The average B-factor of the nucleotides in six ATPase subunits fitted to the
1466 cryo-EM densities of states $E_{D0.1}$ to $E_{D1.3}$ and computed by Phenix in real-space refinement
1467 procedure[51]. The high B-factor of ADP fitted in RPT5 indicates its low occupancy or unstable
1468 association and suggests that the ADP in RPT5 undergoes dissociation in this process.

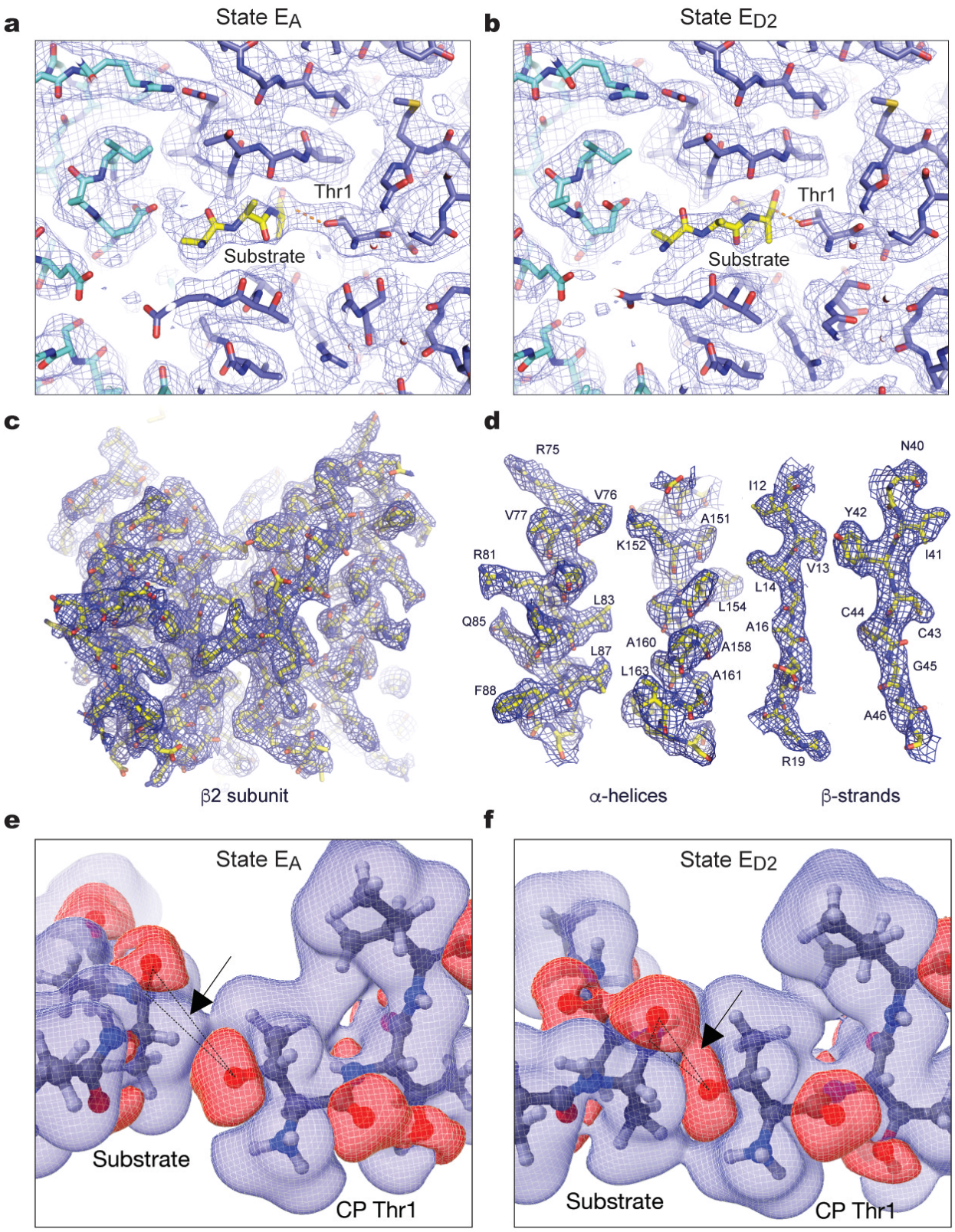

Extended Data Fig. 12. Detailed structural features in substrate interactions in the CP of different gate states. a, The atomic model of substrate-bound catalytic active site of the β2-

subunit superimposed with the cryo-EM density map of state E_A at 2.7 Å. **b**, The atomic model of substrate-bound catalytic active site of the β2-subunit superimposed with the cryo-EM density map of state E_{D2} at 2.5 Å. **c**, Closeup view of the cryo-EM density of the β2-subunit in state E_{D2} shown in blue mesh representation superimposed with the atomic model. **d**, Cryo-EM densities of the typical secondary structure elements in the β2-subunit of state E_{D2} shown as blue mesh representation superimposed with their corresponding atomic models. The residues are labelled. The densities are shown at 4σ level and exhibit structural features consistent with 2.5-Å resolution. **e** and **f,** 3D Charge density difference map showing the interactions between the substrate polypeptide and the residue Thr1 in the β2-subunit of the CP. The red color labels an iso-surface of charge increase while the blue color labels charge decrease, both at a level of 0.04 e/Å^2. The charge increase region at the Thr1-Oγ atom is elongated sideways, and the substrate position in the E_{D2} state provides both a proximity and orientation alignment for the pair to interact. The dashed line triangle shows the plane in which the detailed charge difference contours are plotted as shown in Fig. 6c, d.

Extended Data Table 1. Hyperparameters of the deep residual networks in the 3D autoencoder. Optimizer: Adam. Epochs: 50. Initial learning rate: 0.01. A factor of 0.1 and patience of 3 means that the learning rate will times 0.1 (factor) if the loss function does not improve in 3 (patience) epochs. Batch size: 32 (for the three simulated datasets), 8 (for the substrate-bound proteasome dataset).

Layer name	Output size (simulation)	Output size (proteasome)	Network structure
Conv1	$200 \times 200 \times 200$	$300 \times 300 \times 300$	$5 \times 5 \times 5, 2$
Conv2_x	$100 \times 100 \times 100$	$150 \times 150 \times 150$	$3 \times 3 \times 3, 2$, stride 2 $3 \times 3 \times 3, 2$
Conv3_x			$3 \times 3 \times 3, 2$ $3 \times 3 \times 3, 2$
Conv4_x	$50 \times 50 \times 50$	$75 \times 75 \times 75$	$3 \times 3 \times 3, 1$, stride 2 $3 \times 3 \times 3, 1$
Conv5_x			$3 \times 3 \times 3, 1$ $3 \times 3 \times 3, 1$
Conv6_x (encoding)			$3 \times 3 \times 3, 1$ $3 \times 3 \times 3, 1$
TransConv7_x	$100 \times 100 \times 100$	$150 \times 150 \times 150$	$3 \times 3 \times 3, 1$, stride 2 $3 \times 3 \times 3, 1$
TransConv8_x			$3 \times 3 \times 3, 1$ $3 \times 3 \times 3, 1$
TransConv9_x	$200 \times 200 \times 200$	$300 \times 300 \times 300$	$3 \times 3 \times 3, 2$, stride 2 $3 \times 3 \times 3, 2$
TransConv10_x			$3 \times 3 \times 3, 2$ $3 \times 3 \times 3, 2$
TransConv11			$5 \times 5 \times 5, 1$

1495 **Extended Data Table 2. Cryo-EM data collection, refinement and validation statistics**

	E_A	$E_{A1.1}$	$E_{A1.2}$	$E_{A2.1}$	$E_{A2.2}$	$E_{A2.3}$	$E_{B.1}$	$E_{B.2}$
Data collection and processing								
Magnification	105,000	105,000	105,000	105,000	105,000	105,000	105,000	105,000
Voltage (kV)	300	300	300	300	300	300	300	300
Electron exposure (e–/Å^2)	44	44	44	44	44	44	44	44
Defocus range (μm)	-0.6 to -3.5	-0.6 to -3.5	-0.6 to -3.5	-0.6 to -3.5	-0.6 to -3.5	-0.6 to -3.5	-0.6 to -3.5	-0.6 to -3.5
Pixel size (Å)	0.685	0.685	0.685	0.685	0.685	0.685	0.685	0.685
Symmetry imposed	C1	C1	C1	C1	C1	C1	C1	C1
Initial particle images (no.)	3,254,352	3,254,352	3,254,352	3,254,352	3,254,352	3,254,352	3,254,352	3,254,352
Final particle images (no.)	339,327	192,219	2,539	147,108	5,500	5,842	173,931	9,754
Map resolution (Å)	2.7	2.9	7.5	3.2	6.0	4.8	3.1	4.7
FSC threshold	0.143	0.143	0.143	0.143	0.143	0.143	0.143	0.143
Map resolution range (Å)	2.5-8.0	2.5-8.0	7.0-20.0	2.5-8.0	5.5-20.0	3.0-8.0	2.5-8.0	4.5-20.0
Refinement								
Initial model used	6MSB	6MSB		6MSD			6MSE	
Model resolution (Å)	3.2	3.4		3.5			3.4	
FSC threshold	0.5	0.5		0.5			0.5	
Model resolution range (Å)	2.5-8.0	2.7-8.0		3.0-8.0			2.9-8.0	
Map sharpening *B* factor (Å^2)	-25	-28		-30			-30	
Model composition								
Non-hydrogen atoms	63654	104938	105088	105426	106630	106028	105147	106351
Protein residues	8203	13391	13543	13418	13570	13494	13400	13552
Ligands	11	12	12	12	12	12	9	9
B factors (Å^2)								
Protein	131.13	145.9	145.9	151.26			182.77	
Ligand	125.87	110.13	110.13	108.00			123.85	
R.m.s. deviations								
Bond lengths (Å)	0.008	0.007	0.007	0.006	0.006	0.006	0.006	0.006
Bond angles (°)	0.908	1.013	1.013	1.005	1.005	1.005	1.017	1.017
Validation								
MolProbity score	1.49	1.76	1.76	1.76	1.76	1.76	1.83	1.83
Clashscore	2.72	4.86	4.86	4.91	4.91	4.91	5.57	5.57
Poor rotamers (%)	0.47	0.54	0.54	0.5	0.5	0.5	0.46	0.46
Ramachandran plot								
Favored (%)	93.3	91.34	91.34	91.42	91.42	91.42	90.89	90.89
Allowed (%)	6.52	8.36	8.36	8.33	8.33	8.33	8.77	8.77
Disallowed (%)	0.18	0.3	0.3	0.25	0.25	0.25	0.34	0.34

1496

1497

1498

1499

1500

1501

1502 **Cryo-EM data collection, refinement and validation statistics (continued)**

	$E_{B.3}$	E_{C1}	E_{C2}	$E_{D0.1}$	$E_{D0.2}$	$E_{D0.3}$	$E_{D1.1}$	$E_{D1.2}$
Data collection and processing								
Magnification	105,000	105,000	105,000	105,000	105,000	105,000	105,000	105,000
Voltage (kV)	300	300	300	300	300	300	300	300
Electron exposure (e–/Å^2)	44	44	44	44	44	44	44	44
Defocus range (μm)	-0.6 to -3.5	-0.6 to -3.5	-0.6 to -3.5	-0.6 to -3.5	-0.6 to -3.5	-0.6 to -3.5	-0.6 to -3.5	-0.6 to -3.5
Pixel size (Å)	0.685	0.685	0.685	0.685	0.685	0.685	0.685	0.685
Symmetry imposed	C1	C1	C1	C1	C1	C1	C1	C1
Initial particle images (no.)	3,254,352	3,254,352	3,254,352	3,254,352	3,254,352	3,254,352	3,254,352	3,254,352
Final particle images (no.)	5,117	68,506	77,545	25,755	105,081	169,522	92,777	174,114
Map resolution (Å)	6.1	3.4	3.3	3.9	3.3	3.2	3.3	3.2
FSC threshold	0.143	0.143	0.143	0.143	0.143	0.143	0.143	0.143
Map resolution range (Å)	5.5-20.0	2.5-8.0	2.5-8.0	3.0-8.0	2.5-8.0	2.5-8.0	2.5-8.0	2.5-8.0
Refinement								
Initial model used		6MSG	6MSH	6MSH	6MSH	6MSH	6MSJ	6MSJ
Model resolution (Å)		3.4	3.8	4.3	4.1	4.0	3.9	3.8
FSC threshold		0.5	0.5	0.5	0.5	0.5	0.5	0.5
Model resolution range (Å)		3.2-8.0	3.1-8.0	3.7-8.0	3.1-8.0	3.0-8.0	3.1-8.0	3.0-8.0
Map sharpening *B* factor (Å^2)		-35	-35	-40	-35	-30	-35	-30
Model composition								
Non-hydrogen atoms	105749	104415	103729	105343	105343	105343	105343	105343
Protein residues	13476	13314	13236	13488	13488	13488	13488	13488
Ligands	9	9	5	11	11	11	11	11
B factors (Å^2)								
Protein		174.88	178.15	167.88	213.61	211.63	148.64	165.65
Ligand		143.96	106.39	268.45	208.40	183.93	154.06	175.01
R.m.s. deviations								
Bond lengths (Å)	0.006	0.005	0.007	0.006	0.008	0.006	0.008	0.005
Bond angles (°)	1.017	0.888	0.980	1.079	1.115	1.027	0.987	0.893
Validation								
MolProbity score	1.83	1.65	1.73	2.44	2.47	2.28	2.45	2.45
Clashscore	5.57	4.17	4.39	18.24	18.78	16.38	18.97	17.86
Poor rotamers (%)	0.46	0.4	0.62	0.36	1.47	0.96	1.37	1.68
Ramachandran plot								
Favored (%)	90.89	91.88	91.97	89.47	89.31	89.58	89.09	90.79
Allowed (%)	8.77	7.91	7.82	10.17	10.32	10.1	10.78	8.99
Disallowed (%)	0.34	0.21	0.21	0.36	0.37	0.32	0.13	0.22

1503

1504

1505

1506

1507

1508

1509

1510 **Cryo-EM data collection, refinement and validation statistics (continued)**

	$E_{D1.3}$	E_{D2}	$E_{D2.2}$	$E_{D2.3}$	$E_{A1.RPN1}$	$E_{D.\alpha5}$
Data collection and processing						
Magnification	105,000	105,000	105,000	105,000	105,000	105,000
Voltage (kV)	300	300	300	300	300	300
Electron exposure (e–/Å^2)	44	44	44	44	44	44
Defocus range (μm)	-0.6 to -3.5	-0.6 to -3.5	-0.6 to -3.5	-0.6 to -3.5	-0.6 to -3.5	-0.6 to -3.5
Pixel size (Å)	0.685	0.685	0.685	0.685	1.37	0.685
Symmetry imposed	C1	C1	C1	C1	C1	C1
Initial particle images (no.)	3,254,352	3,254,352	3,254,352	3,254,352	3,254,352	3,254,352
Final particle images (no.)	146,506	856,683	24,674	6,192	128,161	131,570
Map resolution (Å)	3.2	2.5	3.7	7.0	3.7	3.1
FSC threshold	0.143	0.143	0.143	0.143	0.143	0.143
Map resolution range (Å)	2.5-8.0	2.5-4.8	3.0-8.0	6.0-20.0	3.0-8.0	2.5-10.0
Refinement						
Initial model used	6MSJ	6MSK	6MSK		6MSK	6MSK
Model resolution (Å)	3.9	3.2	3.5		3.8	3.6
FSC threshold	0.5	0.5	0.5		0.5	0.5
Model resolution range (Å)	3.0-8.0	2.5-5.8	3.5-8.0		3.5-8.0	2.9-5.8
Map sharpening *B* factor (Å^2)	-30	-20	-40		-100	-25
Model composition						
Non-hydrogen atoms	63654	105218	107626	106422	7717	107626
Protein residues	8203	13420	13724	13572	994	13724
Ligands	11	11	11	11		11
B factors (Å^2)						
Protein	178.66	102.99	182.3		141.87	162.57
Ligand	187.12	116.74	162.17			135.00
R.m.s. deviations						
Bond lengths (Å)	0.005	0.004	0.005	0.005	0.005	0.007
Bond angles (°)	0.913	0.810	1.033	1.033	0.837	1.088
Validation						
MolProbity score	2.32	1.84	1.84	1.84	3.41	1.88
Clashscore	17.69	5.48	5.48	5.48	24.57	6.09
Poor rotamers (%)	0.47	0.69	0.69	0.69	12.01	0.73
Ramachandran plot						
Favored (%)	89.29	90.16	90.16	90.16	81.98	90.17
Allowed (%)	10.36	9.35	9.35	9.35	17.51	9.4
Disallowed (%)	0.34	0.49	0.49	0.49	0.51	0.43

1511